DAMAGE DETECTION OF A THREE-DIMENSIONAL, NON-PLANAR CARBON FIBER COMPOSITE STRUCTURE VIA ELECTRICAL IMPEDANCE TOMOGRAPHY

by

Kelsey Efren De La Trinidad

A Thesis

Submitted to the Faculty of Purdue University

In Partial Fulfillment of the Requirements for the degree of

Master of Science in Aeronautics and Astronautics

School of Aeronautics and Astronautics
West Lafayette, Indiana
December 2025

THE PURDUE UNIVERSITY GRADUATE SCHOOL
STATEMENT OF COMMITTEE APPROVAL

Dr. Tyler Tallman, Chair

School of Aeronautics and Astronautics

Dr. Fabio Semperlotti

School of Mechanical Engineering

Dr. Dianyun Zhang

School of Aeronautics and Astronautics

Approved by:

Dr. Dengfeng Sun

For Victoria, Dipper, and Wendy

ACKNOWLEDGMENTS

I first want to thank Dr. Tyler Tallman for being my advisor. Throughout my graduate studies Dr. Tallman has given the support and encouragement necessary to accomplish my academic goals. I am grateful to have been a part of Dr. Tallman's research group where I grew immensely as a researcher.

Additionally, I wish to thank Dr. Fabio Semperlotti and Dr. Dianyun Zhang for being part of my defense committee and for giving their insights.

I also want to thank all of my fellow lab mates and lab alumni for their technical help, emotional support, and friendship. Everyone has become lifelong friends to me.

Finally, I wish to thank Sandia National Laboratories for funding my graduate studies through the Critical Skills education program. I also want to thank my team at Sandia for understanding the difficulties of doing graduate studies and *almost* full time work. Their flexible has made my time at Purdue possible and I am ever thankful.

TABLE OF CONTENTS

LIST OF TABLES

LIST OF FIGURES

ABBREVIATIONS

BVID	Barely Visible Impact Damage
CEM	Complete Electrode Model
CFRP	Carbon Fiber Reinforced Polymer
EIT	Electrical Impedance Tomography
NDE	Non-Destructive Evaluation
MWCNT	Multi-Walled Carbon Nanotube
GFRP	Glass Fiber Reinforced Polyer
CNT	Carbon Nanotube
CF	Carbon Fiber
PDIPM	Primal-Dual Interior Point Method

ABSTRACT

Composites like carbon fiber reinforced polymers (CFRPs) are heavily leveraged in the aerospace industry, where maximizing structural strength and minimizing weight are a concern. A disadvantage of CFRPs is that they can develop barely visible impact damage (BVID) that degrades performance and require nondestructive evaluation (NDE) methods for effective identification. It would be beneficial to the design engineer and/or end-user if the damage could be detected sooner so that proactive, instead of reactive, actions can be taken to address the damage. Embedded sensing systems could fill this gap by having a method of assessing the health of the composite structure in-situ. The implementation of external sensors are likely not feasible options due to the added complexities, higher costs and increased weight. Therefore, a self-sensing material could be the solution to these obstacles.

Several conductive materials that posses the piezoresistive effect have been investigated for the purposes of detection damage. Piezoresistive materials have a direct electrical response due to applied strains or deformations to the material. In other words, the resistivity of the material increases as the electrical network is perturbed by an external stimuli. Irreversible changes in resistivity are therefore indicators of damage within the material, due to severed internal connections. Nanomaterials like carbon nanotubes (CNTs) and carbon black (CB) have been popular piezoresistive materials because they can electrically functionalize insulating materials, like cement mortars and glass fiber reinforced polymers (GFRPs). However, using these materials require additional processing steps to be effective sensors. The use of conductive nanomaterials is an open research area and can be a barrier for adoption by industry. Conversely, CFRPs are a piezoresistive material that is standard to the aerospace industry. CFRPs do not require modification for self-sensing capabilities and have been demonstrated in damage detecting applications.

Electrical impedance tomography (EIT) is a potential modality for self-sensing within CFRPs due to the ability to detect damage through a current-voltage relationship within the laminate. EIT has been demonstrated as an effective damage detection method for a variety of materials, including nanomaterials and CFRPs. The added benefit of EIT is that the damage is not just *sensed*, but also spatially localized. However, a lot of EIT research

centers on the application to flat plates, do not use fabrics pre-impregnated with resin, and use conductively isotropic materials. However, these examples do not represent the types of materials used in the aerospace industry today.

Presented in this thesis is the application of EIT on a non-planar and geometrically complex prepreg CFRP laminate. A formulation that incorporates the anisotropy of the material is implemented. The conductivity of the material system was experimentally derived. Additionally, EIT reconstructions were also explored using a homogeneous best-fit conductivity, calibrated using initial experimental data and compared with the measurement approach. Two different injection schemes are proposed and evaluated in order to address the increased geometric complexities of the specimen geometry. EIT is an ill-posed and underdetermined inverse problem. This work utilizes two different minimization approaches, namely minimizing the ℓ_1-norm and ℓ_2-norm to the impact of reconstruction images. With this framework in mind, damage from a notch and two impact events were reconstructed using EIT. The notch damage was clear and distinct. A 18 (J) damage reconstruction was stymied by significant noise that prevents definitive identification of the damage. Then a 46 (J) damage detected with significant improvement, but still contained minor noise. Changing the EIT minimization to the ℓ_1-norm dramatically improved the damage reconstruction and eliminated all noise. Damage to the electrode array was likely the sources of noise, which was supported by the results. Nonetheless, the application of EIT to the CFRP specimen demonstrated damage detection capabilities, with limitations that need addressing in order to improve the quality of results. The results of this study indicate a promising approach for using self-sensing CFRPs for an embedded-sensing system.

1. INTRODUCTION

Carbon fiber reinforced polymer (CFRP) composites are attractive materials of choice in the aerospace industry due to their high strength-to-weight ratios, their innate environmental protection, and the ability to be shaped for complex geometries. However, composites can be prone to unique defects or damages not present in traditional metal materials. These types of damages negatively affect the composite laminate by degrading their mechanical performance. Sources of damage can range from manufacturing defects like inter-laminar voids to service damage produced from mishandling [1]. The difficulty is in identifying composite damage before it becomes an issue in normal operating conditions. As high as 30% of composites contain defects due to manufacturing, which become weak points for future damage [2]. In a production environment, composites go through quality control processes to identify these defected parts before going into service or sold to the customer. However, those in-use composites can develop damage during service and the challenge becomes identifying it before a catastrophic failure.

Composites are often laminates made of multiple bonded layers of inhomogeneous materials. These discrete interfaces can be prone to inter-laminar damages, such as fiber breakages, matrix cracking, and delamination. When these failure modes occur beneath the surface layers, they are undetectable via visual inspection. Inter-laminar damage is often due to overloading or through low to high velocity impact damage. The prevalence of this scenario has necessitated the nomenclature of barely visible impact damage (BVID). Common impacts in the commercial aviation industry come from rocks, dropped tools from maintenance personnel or bird strikes. According to the United States Federal Aviation Administration (FAA) wildlife strike database of domestic flights, 18,394 bird strikes were reported in 2023 alone, with an increasing trend year-over-year [3]. As the use of composites continue to increase in the aviation industry and beyond, the ability to effectively identify BVID helps ensure safety of human life and potentially save the destruction of costly products.

Damage detection within a composite structure is critical to the designer or end–user in order first identify and properly prognosticate the damage. Several non-destructive evaluation (NDE) methods have been developed for non-visual damage detection, like ultrasonics, radiography and digital image correlation (DIC) [4, 5]. Electromagnetic waves have been used with cementitous composites for civil applications [6]. Lamb waves frequencies, optical fiber bragg gratings (FBGs), thermography, and vibrational techniques have all been used to characterize composites [7, 8]. However, these methods typically require external sensors, specialized equipment, well-trained personnel and physical access to the structure itself. Additionally, these detecting modalities are often conducted in a controlled environment where the unit under test (UUT) is not in service. Therefore, there is currently a gap in capabilities when products containing composite structures like CFRPs are in use.

An attractive approach to addressing this gap is to have an embedded sensing system within a composite structure to provide "state–of–health" information instead of traditional NDE methods. The advantage with this approach is that the required sensing equipment is already integrated within the composite with the structure therefore serving the multifunctional role of a diagnostic sensor for the engineer or end–user. Embedded sensing systems can be purposed for a range of uses, such as thorough diagnostic software during maintenance or to trigger a user notification alert that an issue needs addressing. The sensors selected can also be tailored to the desired information. Embedded sensors in composites have been used to measure various properties like pressure, strain, temperature, and mechanical loading [9–12]. This flexibility makes embedded sensing systems appealing due to the various approaches, types of data sensed, and their applications in composites.

However, physically embedded sensors pose an additional set of challenges for composite structures. These challenges stem from the additional manufacturing labor burdens, potential reduction in mechanical performance due to inhomogeneous sensor integration, difficulty powering electronics, and achieving uniform sensor coverage [13]. Another embedded sensing approach is to use self-sensing materials and forego the inclusion of additional sensors [14]. Graphene-based nanomaterials (GBN) that have been mixed with the mortar of cementitous composites were able to detect physical deformation [15]. Thin sensing films have been an effective approach towards uniform sensor coverage. Electrically conductive thin films made from multi-walled carbon nanotubes (MWCNTs) have been integrated into glass fiber reinforced polymer (GFRP) composites and wearable fabrics for strain-sensing capabilities [16, 17]. Carbon black (CB) is another nanomaterial that can be mixed into traditionally insulated materials like epoxy or cement to add deformation detecting capabilities [18–20]. Additionally, carbon fiber itself has been demonstrated to have sensitivity to deformations in a variety of forms, from individual fibers to laminates [21–23]. Considerable research has gone into characterizing different materials for self-sensing applications to form non-intrusive systems that alleviate the disadvantages of discrete sensors.

1.1 Piezoresistive Sensing Materials

The basis of many self-sensing materials rely on the piezoresistive effect, where mechanical strain gives rise to a change in electrical resistivity of the material. In practice, a measurable change in resistance is directly related to a change in the strained state of the material. Another property of these materials is that they often have ohmic behavior, meaning there is a linear relationship between current and voltage. Ohmic behavior is advantageous for self-sensing materials because it means the electrical response is predicable. However, not all self-sensing materials are ohmic and do exhibit nonlinearity. These materials create an electrically connected network with an initial resistivity. As strain or damage is imparted into the sensing material, an irreversible resistivity change occurs, indicating permanent plastic deformation. When incorporated into a specimen or laminate structure, measured resistance changes can be calibrated for strain data, used as an indicator of damage, or used in some other empirical model.

A popular piezoresistive material is the carbon nanotube (CNT). CNTs have the ability to electrically functionalize a non-conductive material like GFRP and cement. These conductive nanofillers form an electrically connected network within the material when they are dispersed at a low volume fractions beyond a percolation threshold. As seen in Fig. (1.1), these networks can be categorized into Type I and Type II configurations [24]. Type I involves physical overlapping of the conductive nanofillers and Type II is characterized as in-plane contact. The small separation distances between proximal CNTs have an electrical tunneling effect to bridge these gaps to form conductive connections. These conductive networks are dependent solely on the nanofillers and thus when the configuration of nanofillers change, the material's resistivity changes. This behavior lends itself well to detecting strain and damage within a composite. In general, as individual nanofillers begin to separate, the resistivity of the network increases. Conversely, if the separation distance between individual nanofillers decrease, the resistivity decreases. This behavior correlates well to deformations due to tensile or compressive strains respectively. Consequently, physical damage severs connections within the electrical network and lower conductivity of the material.

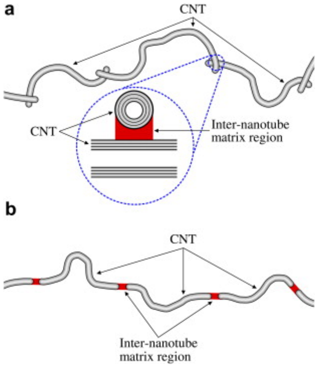

Figure 1.1. CNT networks dominated by (a) overlapping contact configuration (Type I) and (b) in-plane contact configuration (Type II). [24]

Much research has gone into characterizing CNT modifiers for sensing capabilities. In Esmaeli et. al [25], an epoxy matrix was modified using single and double walled carbon nanotubes (SWCNTs, DWCNTs) in 0.5-0.75 wt.% and subjected to tensile and fracture loading. The following process is representative for manufacturing a nanofiller-modified matrix and are the steps taken by the authors. The nanofillers were added to an aqueous solution, sonicated for 30 minutes, degassed under vacuum for 30 minutes, a surfactant agent to aid dispersion, and poured into dog bone and fracture silicone molds. The authors observed a reduced sensitivity and higher nonlinearity in normalized resistance changes under tensile conditions, however, linear behavior was observed for the 0.5 wt.% fracture specimens. As seen in Fig. (1.2), computed tomography (CT) imaging showed the 0.75 wt.% specimen had conglomerates of nanofillers, potentially leading to the results. This work demonstrated the challenge of finding optimal nanofiller wt.% and discovering the undesirable piezoresistive responses like nonlinearity.

In Ku-Herrera and Avilés [26], 0.3 wt.% MWCNTs were used with a vinyl ester resin (VER) to produce dogbone specimens and tested under cyclic tension and compression.

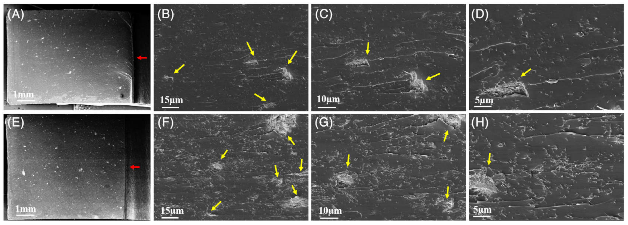

Figure 1.2. Microstructural characteristics at different CNTs loading: A-D, 0.5 wt.%; E-H, 0.75 wt.% (red and yellow arrows indicate direction of crack propagation and CNTs aggregates respectively)(Color figure can be viewed at wileyonlinelibrary.com). [25]

It was observed that there was linear correlation between strain and changes in resistance for cyclic tensile loading. Under compression, the change in resistance indicated distinct behavior between linear-elastic regions, onset matrix yielding, and in the plastic region. It was concluded that a MWCNT/VER material system is sensitive to matrix failure, indicated by the unloaded resistance being larger than the initial value, and can be seen in Fig. (1.3). The authors claimed that the this kind of response makes CNTs a good candidate for smart, self-sensing materials for composites.

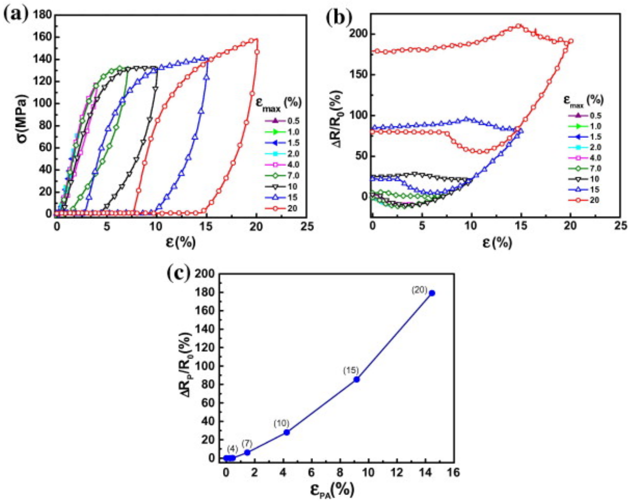

Figure 1.3. Compressive electro-mechanical response of a MWCNT/VER composite under incremental strain cycles. (a) Stress vs. strain, (b) normalized change of electrical resistance vs. applied strain, and (c) permanent change of electrical resistance as a function of plastic accumulated strain. [26]

Carbon black is another popular nanofiller used for self-sensing. CB nanoparticles are produced from the thermal decomposition from petroleum based hydrocarbons. The structure of CB is not as highly ordered like CNTs, and are therefore cheaper to produce than CNTs. It is common among self-sensing materials research to characterize the impact of various material properties on sensing capabilities and how they relate to the mechanical performance. In Nalon et. al [27], the authors sought to characterize commonly used conductive CB nanofillers in cement-based composites; comparing how the inner CB structure affects conductivity and mechanical strength. Resistivity tests were conducted on four cement block samples containing four different commercially available CB nanofillers. These nanofillers differed in their respective surface area per gram, sheet resistivity, and Dibutyl Phthalate (DBP) absorption number, Fig. (1.4). Resulted indicated that increases in surface area per gram, DBP number and lower resistivity produced reliably higher peizoresistive sensitivity. However, cyclic compressive load testing revealed lower compressive strengths compared to the unmodified control specimen. The conclusion form this work was that the various material parameters of CB negatively affected mechanical strength and should be considered when designing a *smart* sensing structure.

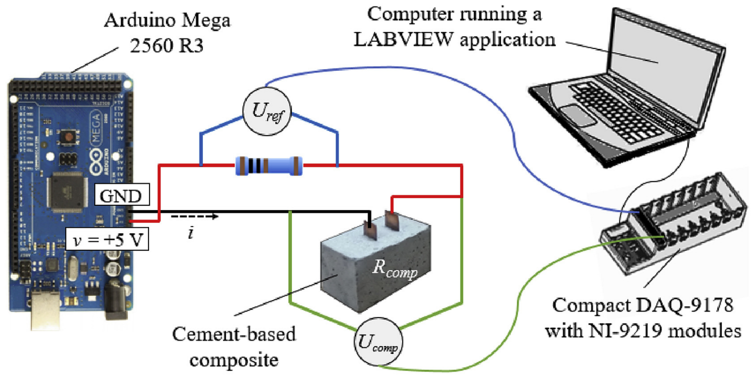

Figure 1.4. Experimental test setup for DC tests. [27]

Carbon fiber (CF) as a raw material also exhibits piezoresistive properties. The benefit of CF compared to previously mentioned self-sensing materials is that no conductive nanofillers are required because the fibers are conductive enough for electrical measurements. An example of unmodified CF sensing was done by Roh and Park [28], where monofiliment and

3K plain-weave tows were electro-mechanically characterized and applied to a grid sensor system. The materials were commercially available and instrumented using silver paste to minimize contact impedance with the sensing equipment. Tensile tests of both the monofilament and 3K tow showed linear relationships with strain. Then, tows were arranged into a grid pattern with varying separation distances within a GFRP laminate. These laminates were subjected to three-point bend tests in different locations with each tow's resistance measured in-situ, Fig. (1.5). Results showed the proximity to strain affected the magnitude of recorded resistance changes, where measured changes decreased with distance from the applied strain. An interesting observation by the authors was that the gauge factor decreased inversely with grid density. This was attributed to lower overall recorded resistance changes. However, the grid was effective at localization of the flexural strains applied. Nishio et. al [29] investigated various plain–weave CFRP laminates with ±45° and 0°/90° fiber angles and the effect of ply count. In the $[\pm 45°]_6$ laminates, cyclic tensile loading produced in-plane shear plastic deformation that reduced the separation distance between fibers in the warp and weft directions, effectively increasing the conductive network. An observed negative piezoresistive effect occurred where the resistance change decreased with applied strain, which was not observed in $[0°/90°]_6$ laminates. The results highlighted the effects of fiber/ply orientation. These works demonstrate the ability of CF to detect deformations, but also have limitations with potentially differing piezoresistive responses depending on loading conditions.

However, there are certain challenges associated with using CF as a self-sensing material, namely that conductivity is anisotropic. A single fiber has less resistivity in the direction along the fibers than in the transverse direction. As an example, Athanasopoulos and Kostopoulos [30] measured rectangular unidirectional (UD) CF laminates and measured resistivity as a function of fiber angle and laminate thickness. Fibers algined with the 0° angle had a resistivity of $3.166\ 10^{-5}\ \Omega m$ and fibers aligned to the 90° direction had a resistivity of $2.632\ 10^{-2}\ \Omega m$. When multiple intermediary angles were measured, a gaussian-like curve was produced from 0° to 180°, as seen in Fig. (1.6). This anisotropy is further exacerbated in the through–thickness direction for CFRP laminates with smaller conductivity. In Guadagno et. al [31], the authors attempted to improve the overall conductivity of CFRPs through adding 0.5 wt.% MWCNTs into the epoxy matrix. As a result the planar conduc-

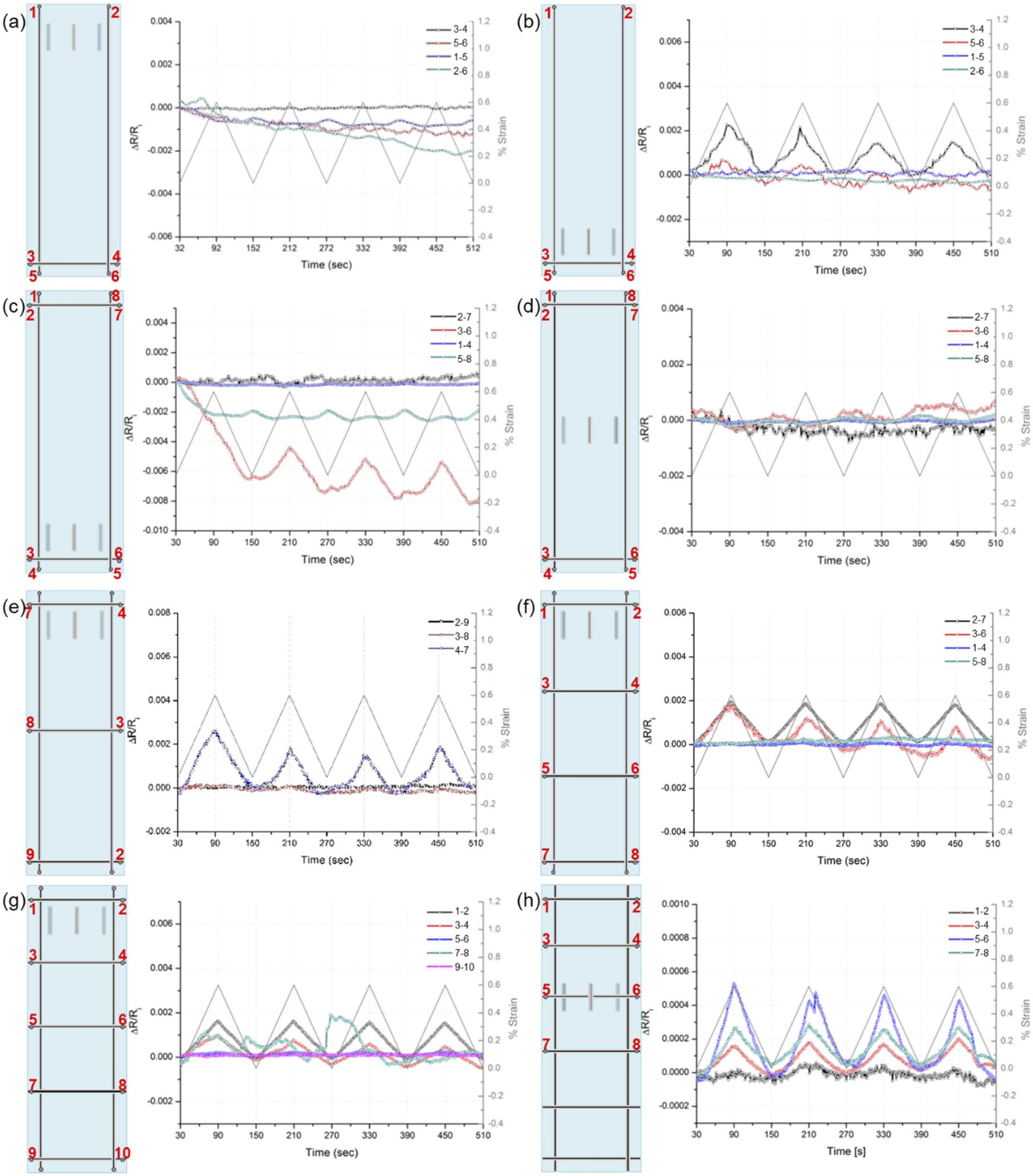

Figure 1.5. Specimen types, loading location, and corresponding electromechanical behaviors. [28]

tivity increased by 72% and the through-thickness conductivity increased by 120% to 19,500 ($\mathrm{S\,m^{-1}}$) and 3.9 ($\mathrm{S\,m^{-1}}$) respectively. Figure (1.7) shows a field emission scanning electron microscope (FESEM) image where the MWCNTs are seen bridging between fibers, leading to the conclusion that the addition of CNTs increased the laminate's conductivity.

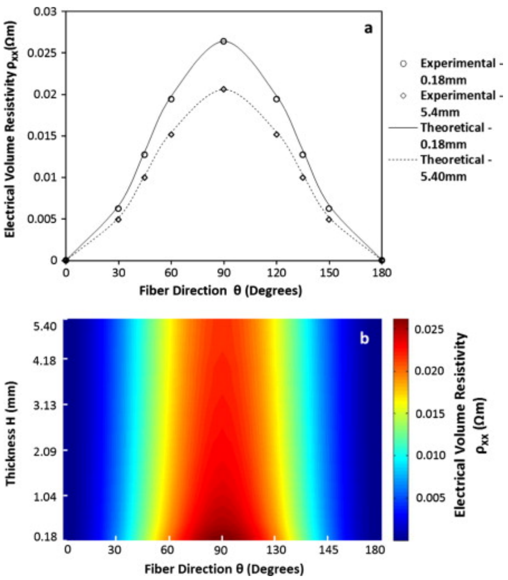

Figure 1.6. (a) Volume resistivity ρ_{xx} as a function on carbon fiber direction (θ) for two different values of thickness (h) and length to width ratio ($\lambda \gg \lambda_{cr}$), and (b) Theoretical VR ρ_{xx} as a function of carbon fiber direction (θ) and the thickness. [30]

There are two common categories of CFs, determined by the method of producing said fibers. The first are polyacrylonitrile (PAN) fibers due to PAN fibers being the precursor for the eventual graphitization of the fibers. The second are meso-phased pitch fibers which are petroleum based. In two studies by Xi and Chung [32, 33], PAN and pitch based piezoresitivities were characterized under tension, Fig. (1.8), and factors like the microscale order of graphitization and tow count did not alter the resistivity of fibers under tension. These results indicate that at a macroscale, the choice of CF type do not affect sensing capabilities, indicating robustness of the material for embedded sensing systems in addition to PAN composites being the most common in the aerospace industry.

A lot of research in piezoresistive materials focused on flat laminates or with dry fibers. Work by Ku-Herrera et. al [34] sought to characterize the piezoresistivity of a CFRP I-beam geometry subjected to cyclic tensile and compressive loading. A 12k uniaxial CFRP was manufactured in the shape of a structural I-beam. The two flanges were comprised of $[0]_6$

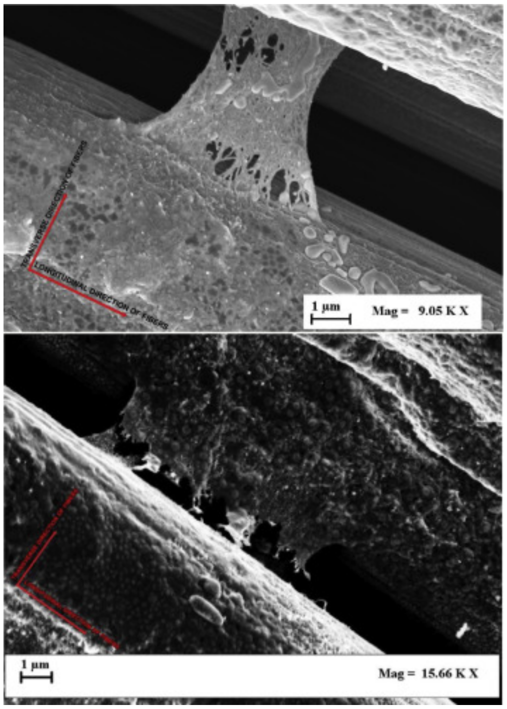

Figure 1.7. FESEM images of the etched panel P2B: the strips have been observed in the section perpendicular to the panel plane. [31]

plies and the web was layered with $[+45°/-45°/+45°]$ on both sides of the web with a pair of electrodes instrumented on the two flange surfaces, Fig. (1.9). Under a four-point bend test, the surface contacting the fixture experiences compression with the opposite surface experiences tension. When the I-beam was subjected to monotonic loading, the compressive surface recorded a negative piezoresistive effect and the tensile surface experienced a positive piezoresistive response. This behavior continued under cyclic flexure loading with increasing increments of magnitudes, Fig. (1.10). When compared to a tested rectangular laminate, the I-beam specimen had a marked lower piezoresistive sensitivity. It was hypothesized that the stiffness and geometry affected the sensitivity of the I-beam specimen. Additionally, irreversible resistance changes were attributed to progressive laminate failure. It was theorized the primary causes were residual stress relief within the laminate, fiber realignment, and finally laminate failure.

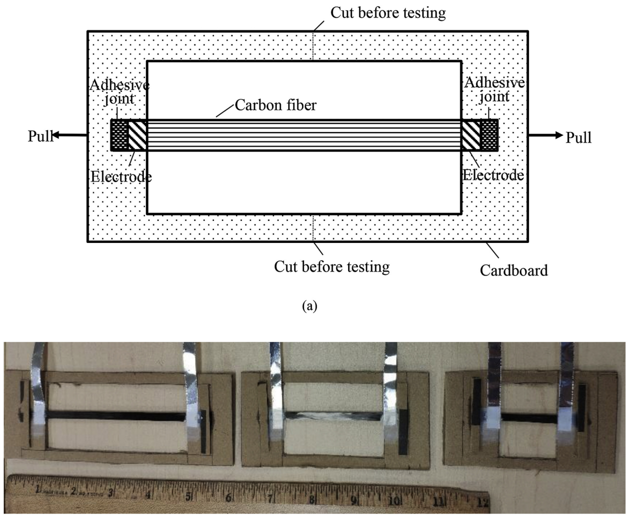

(a)

(b)

Figure 1.8. Testing configuration. (a) Carbon fiber tow mounting for capacitance/voltage measurements during tensile testing. (b) Photograph showing mounted carbon fiber tow (Type A) of three lengths (L, 2L and 3L), along with a ruler with main divisions in inches. (A color version of this figure can be viewed online.) [33]

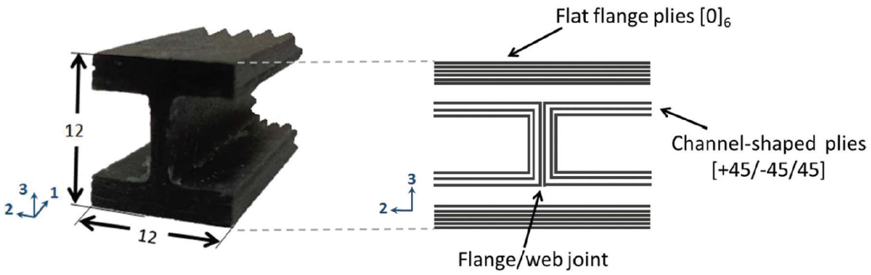

Figure 1.9. Picture of cropped I-shaped specimen (left) and schematic of ply orientations (right). Dimensions in mm (not to scale). [34]

1.2 Damage Detection via EIT

Carbon fiber has been shown to have self-sensing capabilities, either individually or within laminates due to the piezoresistive effect and is a good candidate for embedded sensing systems with the objective of damage detection. CFRPs are already ubiquitous in the aerospace industry, where qualifying a new material with conductive nanofillers may prove too costly. Additionally, technology has become heavily integrated in today's aerospace

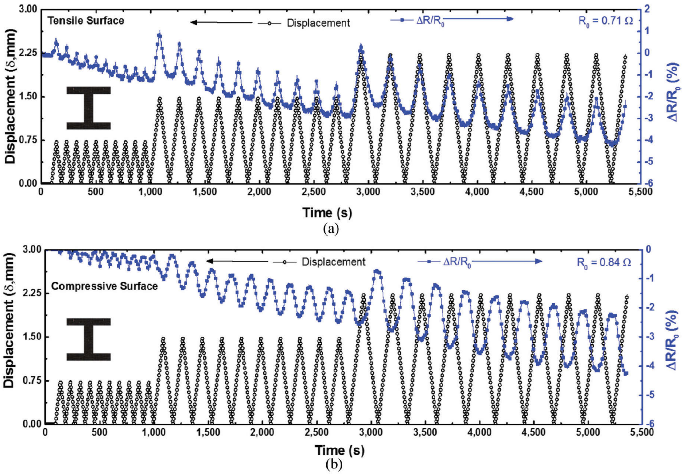

Figure 1.10. Cyclic flexural loading at incremental displacement amplitudes for a representative specimen with I-shaped cross-section on (a) tensile side and (b) compressive side. [34]

landscape where sensor data fusion from an embedded sensing system can guide future aircraft emergency alert systems or help extend the service life of costly aircraft. These factors may make self-sensing embedded systems more palatable for the aerospace industry to investment into this technology.

Ideally, an embedded sensing system would provide engineering strain information. With strains, stresses can be computed within the laminate and evaluated against various composite failure mode theories. Another use for these systems could be the collection of periodic data over time to extract creep displacement. However, the prevailing use of CFRP self-sensing laminates is for damage detection. A resistivity-strain relationship is required to take self-sensing materials beyond damage detection. Work by Koo and Tallman [35] proposed a general higher-order piezoresistivity-strain model for carbon nanofiber (CNF) modified epoxies. By using experimental resistance data and strain gauge data, a piezoresistive model was used to accurately predict displacement as a function of change in resistance. Furthermore, the model was validated against electrical impedance tomography (EIT) data to quantify the model's ability to predict resistance change distributions accurately, Fig. (1.11). The piezoresistivity model had good agreement with experimental data. However, a limitation of this empirically derived model was the calibration corresponded only for a specific range of small strains and a specific material system. While it is possible to create a piezoresistive model for various material systems, it would require additional research and development.

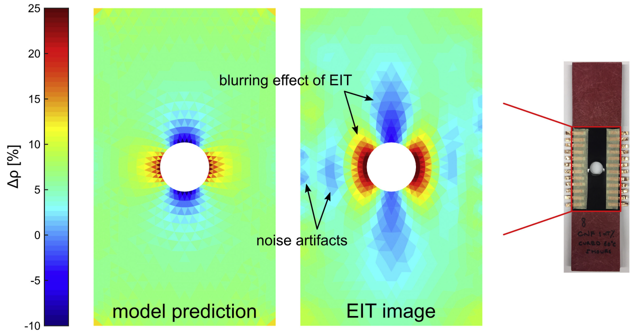

Figure 1.11. Left: model-predicted resistivity changes for a plate in tension with a hole. Note the large resistivity changes which collocate with strain changes, Right: EIT-predicted resistivity change distribution. Despite the EIT-predicted changes and the presence of noise artifacts in the EIT-image, good model-to-experiment agreement is observed. [35]

Prior examples on piezoresistive materials mainly focused on damage detection without refined spatial information. The next step forward from damage detection is damage localization on the laminate. EIT is one such modality that provides a visual representation of damage size and location in relation to the laminate. The goal of EIT is to use the current–voltage information at the boundary of a domain to predict the internal spatially varying conductivity distribution. Some of the earliest development of EIT comes from the field geophysics where Lawrence Livermore National Laboratory (LLNL) staff Lytle and Dines [36] proposed injecting current into an electrode array around a geological core sample to determine electrical conductivity distributions. Concurrently, Henderson and Webster [37] developed an impedance camera system that collected data to produce isoadmittance contour maps of the human thorax. Research has continued to improve on this concept and there now exist advanced systems, like a portable EIT systems proposed by Xu et. al [38]. Another example is the development of a phantom tank instrumented with electrodes, the conductivity change from heating a raw egg over time was visually reconstructed. Other biomedical imaging applications range from lung ventilation monitoring, brain activity, and cardiac blood flow [39–42].

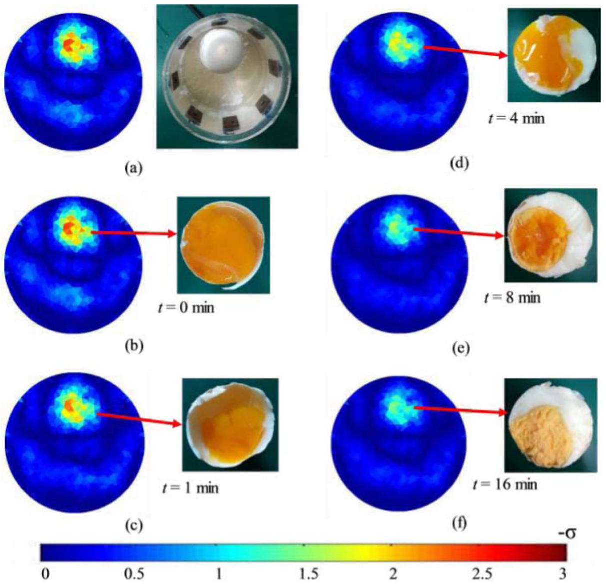

Figure 1.12. Reconstructed Image of egg at 50 KHz. (a,b) Reconstructed images of raw egg. (c, d, e, f) Reconstructed images of egg heated for $t = 1$ min, 4 min, 8 min and 16 min, respectively. [38]

Fields of NDE and structural health monitoring (SHM) motivated the initial push for EIT in structural applications. In works by Loyola et. al [43, 44], a GFRP fabric mat was sprayed with a MWCNT poly(vinylidene flouride) (PVDF) latex film prior to layup for added damage sensing capabilities. EIT reconstructions were done with through-hole and impact damage, ranging from 20 (J) to 140 (J), on the sensing film, Fig. (1.13). In Lestari et. al [45], a similar sensing film was applied to a CFRP tensile specimen where several EIT conductivity change reconstruction images were produced at multiple strained states, Fig. (1.14). Similarly, Heinzlmeier et. al [46] performed EIT on a plain-weave CFRP plate laminate with a screen-printed carbon paste film covering the entire plate. A through-hole was created in the center, was instrumented with edge-mounted electrodes and subjected to cyclic tensile loading. DIC was used to correlate the EIT reconstructions at various cycle counts. The EIT results did not match the DIC results, showcasing the challenges with EIT producing meaningful results in the presence of noise. However, these works indicate a high interest in using EIT for sensing strain or the result of applied strains.

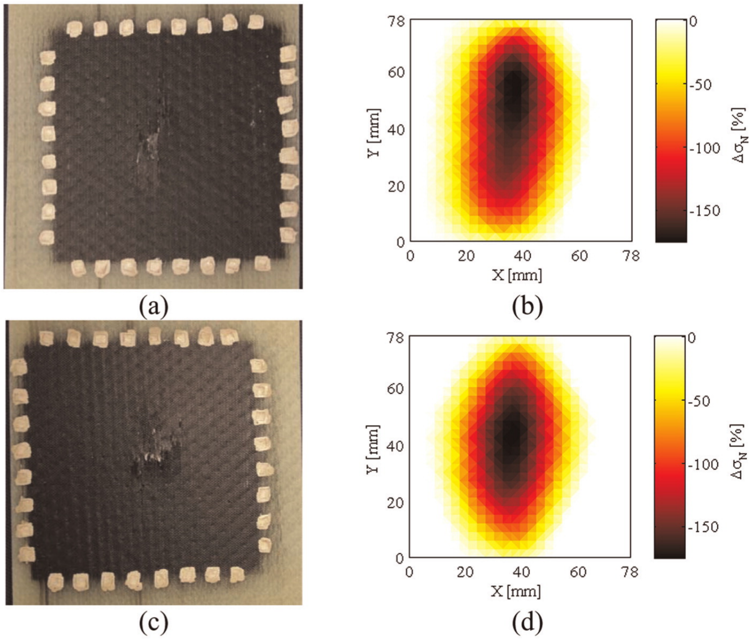

Figure 1.13. GFRP specimens have been subjected to impact testing. (a) The photograph and (b) EIT reconstruction of a specimen subjected to 100 J of impact as shown. (c) The photograph and (d) EIT map of a specimen subjected to 140 J of impact is also shown. [43]

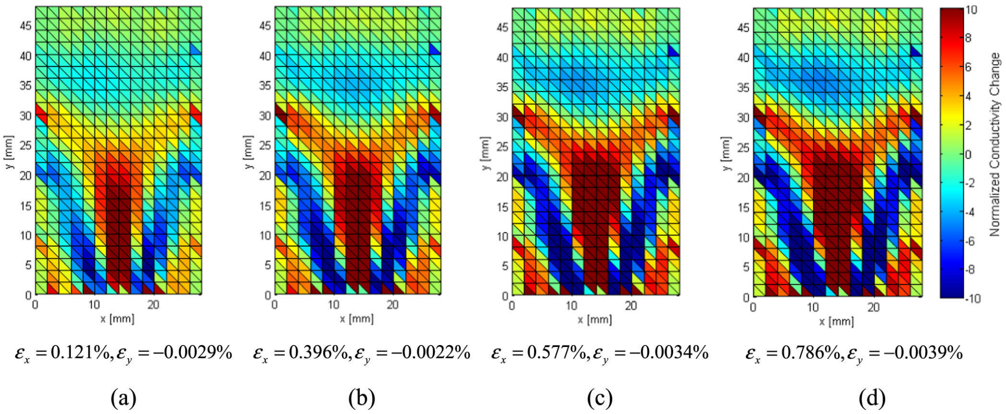

$\varepsilon_x = 0.121\%, \varepsilon_y = -0.0029\%$ (a)

$\varepsilon_x = 0.396\%, \varepsilon_y = -0.0022\%$ (b)

$\varepsilon_x = 0.577\%, \varepsilon_y = -0.0034\%$ (c)

$\varepsilon_x = 0.786\%, \varepsilon_y = -0.0039\%$ (d)

Figure 1.14. Electrical conductivity maps for CFRP sample C2 for varying levels of strain and damage. Figure (6) shows the "location" of these images on the load/strain plots. [45]

Several works have also attempted to integrate machine learning to improve EIT reconstructions images. In work by Hassan et. al [7], a genetic algorithm was used for piezoresistive

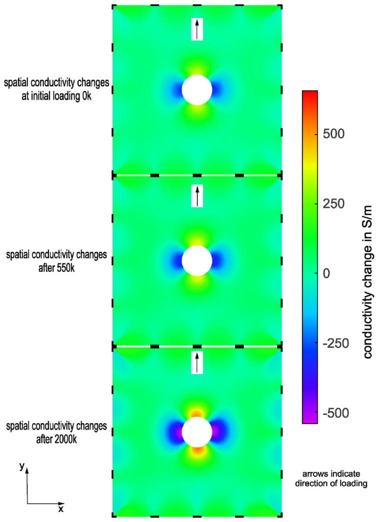

Figure 1.15. Spatial conductivity changes at peak load $S_{\mathrm{max,i}}$ for selected cycles. [46]

inversion to correlate EIT-predicted conductivity changes with displacement of a CNF/epoxy specimen with good comparative results to finite element modeling (FEM) and DIC. Cheng et. al [47] compared traditional and other machine learning methods for EIT reconstructions and namely proposed a Bagging algorithm with transfer learning (BT-CNN) to train the model due to the lack of real training data. Figure (1.16) shows results from various methods like total variation (TV) with the proposed BT-CNN approach for various impacts on a CFRP plate.

Much work in EIT for self-sensing materials has been done on flat plates using a hand-layup manufacturing process of dry fibers or fabrics. Real use of composites like CFRPs are not flat plates and can range from curvilinear forms to more complex structural members. Work by Sannamani et. al [48], applied EIT to a CFRP airfoil with surface mounted electrodes, Fig. (1.17), that was subjected to through-hole and impact damage. This shape is more representative of a possible *real-world* composite structures. Additionally, the surface was instrumented instead of the edges, which is a more preferable location for an embedded sensing system. Conductive anisotropy was also addressed with results implying changes in conductivity are dominated by planar conductivity and not through-thickness conductivity. In another example, work by Thomas et. al [49] applied EIT for multiple through-hole

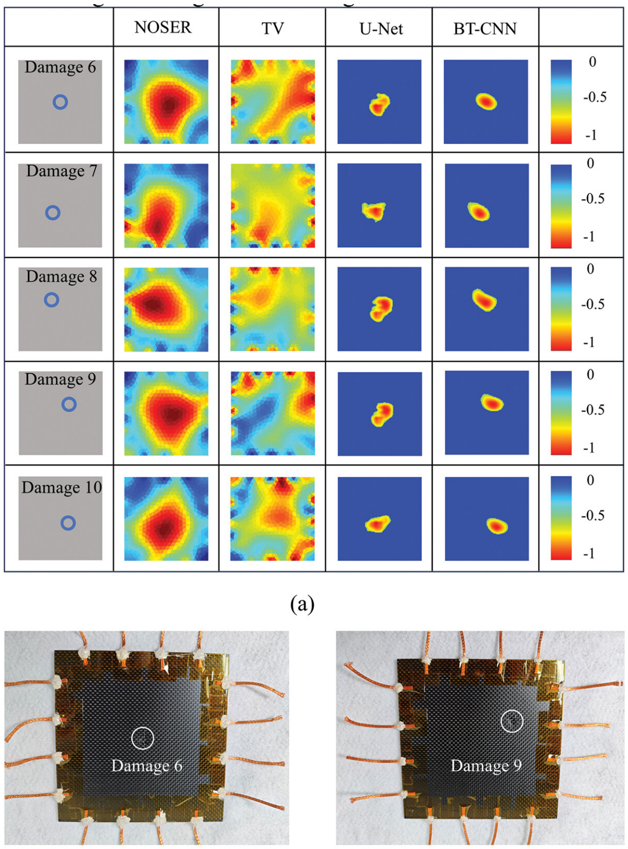

(a)

(b)

(c)

Figure 1.16. (a)Reconstructed images obtained in CFRP real data(b) test specimen plate for damage 6.(c) Test specimen plate for damage 9.(In order not to take up extra space, only two samples are shown.) [47]

and impact damage detections of a CB-modified GFRP tube. Two subsequent low velocity impacts resulting in BVID were successfully identified in EIT reconstruction images, Fig. (1.18). An interesting result were the differences in predicted conductivity loss for the same through-hole size, but at different locations along the tube. The electrode array was edge-mounted and therefore not uniformly spaced along the length of the tube, which could be attributed to the lower sensitivity observed when the hole was further from an electrode. Shu et. al [50] sought to apply EIT to a 3D-printed cellular lattice structure typically plagued by noise and low sensitivity of inner strut members. A strut-based normalization approach helped bring the predicted conductivity losses closer in magnitude for improved sensing and penalized the affect of struts not relevant for damage reconstruction. Figure (1.19) shows how this approach correctly identified the damaged strut. In Tallman et. al [51] an advanced regularization method utilizing both the smoothness prior and conditionally Gaussian prior to precisely detect multiple notch damages in a carbon fiber based, 3D-printed truss structure. A comparison of smoothness prior and mixed prior approaches are shown in Fig. (1.20) where three notches and a cut ligament were reconstructed better with the more advanced regularization. Hussain et. al [52] performed EIT on several CF-based, 3D-printed circular-shaped specimens where specified regions were electrically *activated* or deactivated based on a controllable fiber alignment printing parameter. EIT reconstructions shown in Fig. (1.21) were comparable to traditional through-hole damaged specimens, showing a potential new approach for in-situ monitoring of CFRPs. A final example of recent EIT research on complex geometries was work by Jauhiainen et. al [53], where multiple cracks were introduced to a multi-planar, graphite-based sensing skin. A unique aspect about this work was having the damage span multiple planes of the skin and reconstructed accurately, as seen in Fig. (1.22). These works highlight novel methods for accurate damage detection more complex geometries using EIT and the new challenges to overcome.

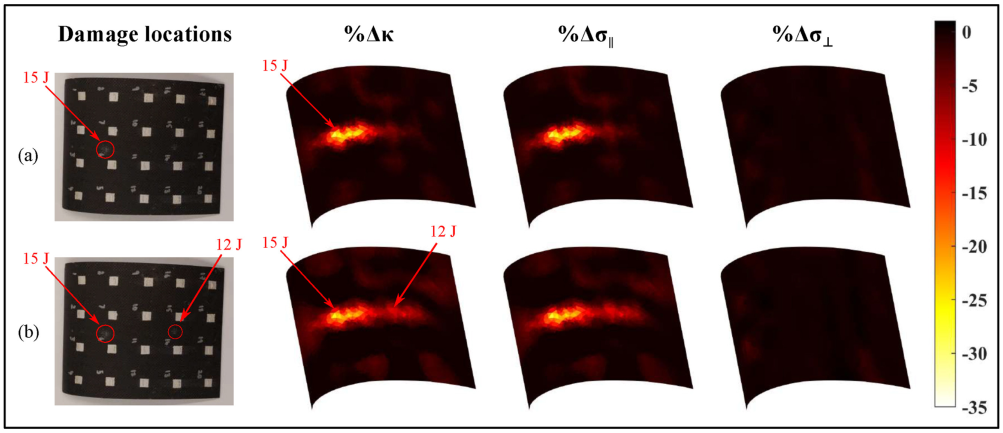

Figure 1.17. EIT reconstruction of (a) just the 15J impact and (b) both the original 15J and the subsequent 12J impact (recall the impacts were at different locations) with respect to $\%\Delta\kappa$, $\%\Delta\sigma_{\parallel}$, and $\%\Delta\sigma_{\perp}$. [48]

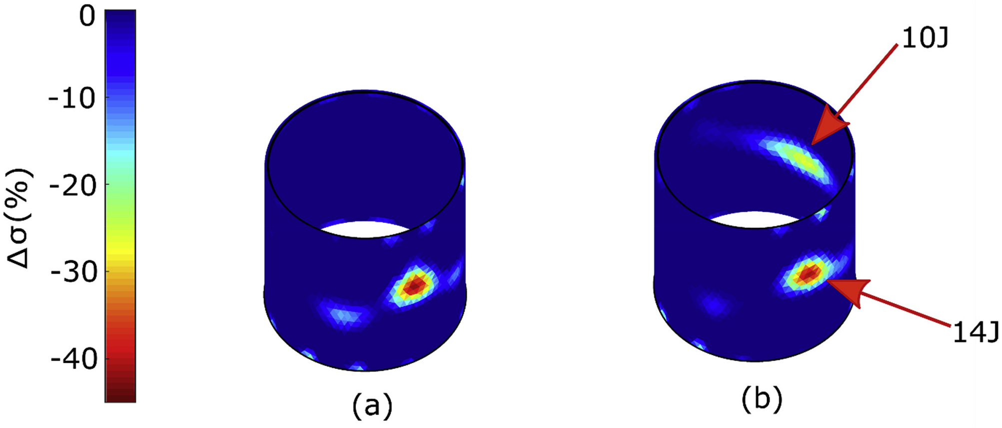

Figure 1.18. EIT reconstruction of the post-impacted tube at (a) 14J and (b) 14J and 10J. [49]

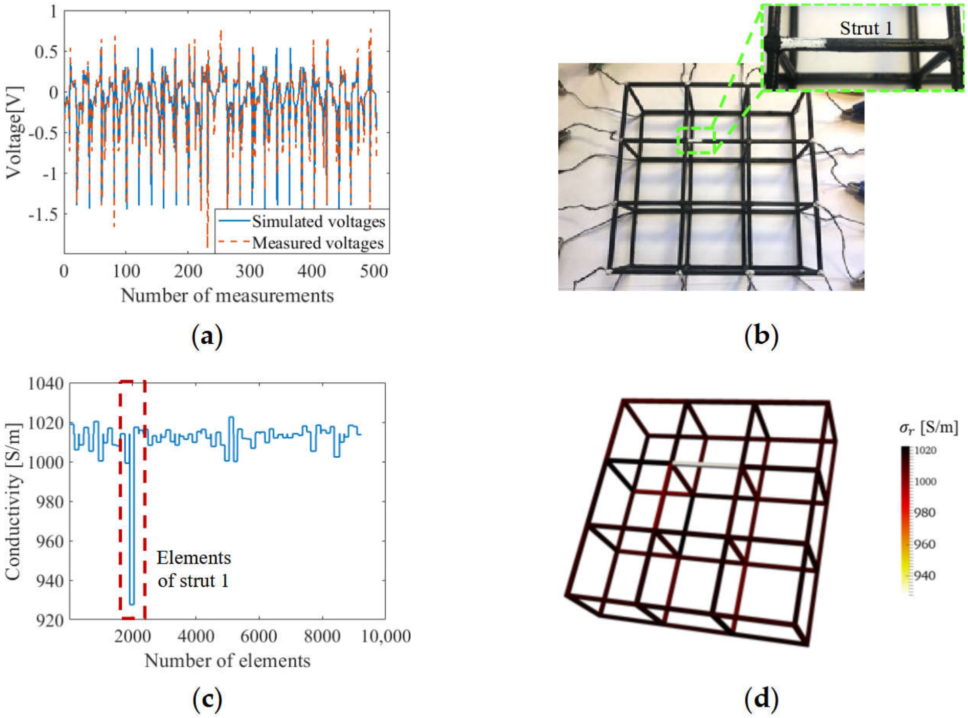

Figure 1.19. (a) Simulated voltages are compared with experimentally measured voltages. (b) The first etch (damage) was introduced in the lattice. (c) The reconstructed conductivity values of each element when solved with the normalized sensitivity map are plotted. (d) The corresponding 3D conductivity distribution successfully confirmed damage detection in strut 1. [50]

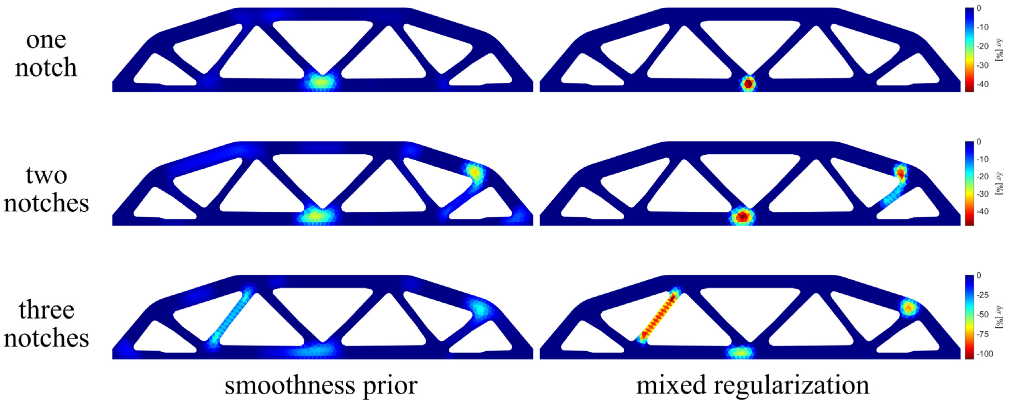

Figure 1.20. Experimental results using the smoothness prior (left column) and the newly proposed mixed regularization (right column). [51]

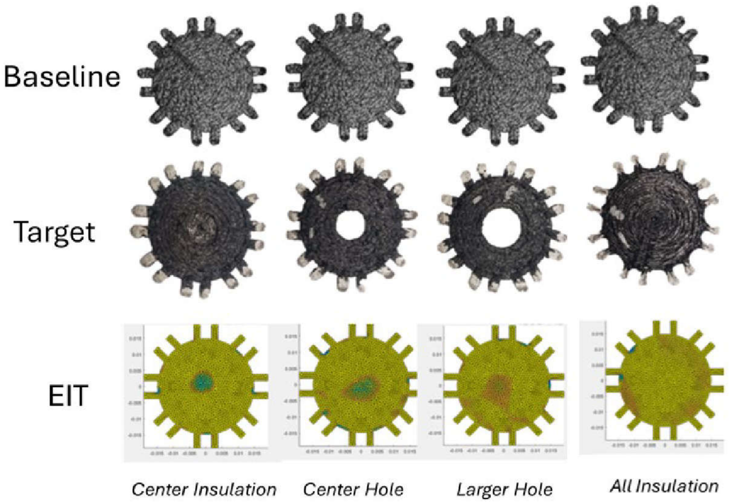

Figure 1.21. EIT results of the samples with insulation and printed hole defects compared to the baseline (all conductive) specimen. [52]

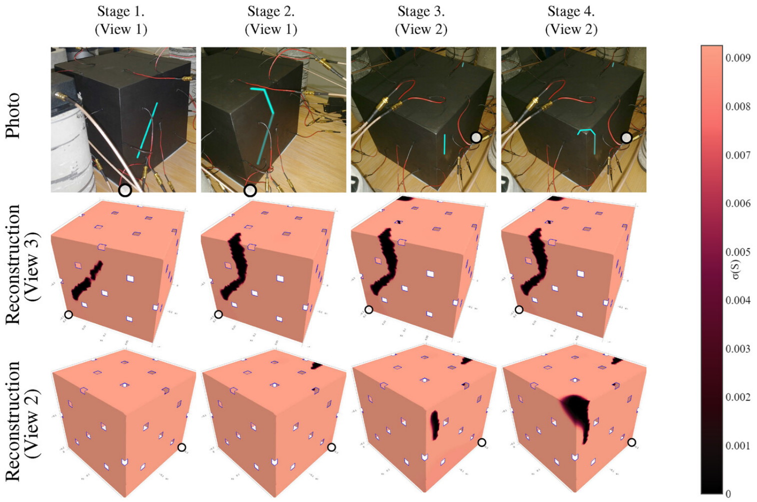

Figure 1.22. Case 4: Photographs of the sensing skin applied on the cubic object in the experimental study (top row) and the respective ERT reconstructions (middle and bottom rows). The photos and reconstructions correspond to four stages of cracking; in the photographs, the cracks at each stage are highlighted and the cracks of the previous stages are darkened. Note that the reconstruction images on the second row also show the side of the cube that has no cracks (View 3). The white circle marks the same corner of the cube in the photographs and in the reconstructions. [53]

2. PROBLEM STATEMENT AND RESEARCH GOALS

The preceding review of self-sensing materials with the application of EIT has largely focused on flat plate composites with only recent research expanding to non-planar geometries. Continued research is required to identify and overcome the challenges of implementing EIT for geometrically complex, resin pre-impregnated (prepreg) composite laminates that are more realistic to real–world structures. Furthermore, carbon fiber prepreg has been under-investigated as a self-sensing material via EIT, instead much of the research focusing on conductive nanofiller-modified materials. With this motivation, the following Problem Statement and Research Goal are stated.

2.1 Problem Statement

CFRPs are attractive materials due to their high strength–to-weight ratio, design flexibility, and inherent corrosion resistance. However, in aerospace applications, CFRPs are prone to BVID while in-service and are typically not identified, if at all, until NDE methods can be performed. To address this gap in capabilities, an embedded self-sensing system is a potential solution where the piezoresistive effect of CFRPs can be used to detect defects like BVID. CFRPs are also a logical choice in self-sensing materials because CFRPs are readily available as commercial-off-the-shelf (COTS) materials and do not require additional steps for electrical functionalization. Demonstrating accurate self-sensing within CFRP prepreg laminates will lower the barrier of entry for embedded self-sensing systems through the use of existing materials, keeping costs down. Furthermore, EIT is potentially a good detection modality for embedded self-sensing system due to proficiencies in detection, localization, and sizing of damage. The CFRP structure only needs an appropriate electrical interconnect, such as from an electrode with no further modifications of the laminate. More research is needed to address current challenges in CFRP damage detection via EIT. First, the anisotropic conductivity of CFRPs needs to be implemented into EIT formulations to accurately reflect resistance changes. Second, EIT needs to be applied to more complex geometries to develop the techniques required for CFRPs designed by engineers. Lastly, minimal EIT research has involved prepreg carbon fiber and is dominated by the wet hand layup of dry fabrics. Use of dry fabrics is reasonable in a laboratory environment, but industry almost exclusively uses prepreg sheets when manufacturing laminates. The EIT state-of-the-art needs to be demonstrated as an effective damage detecting modality of complex geometries using prepreg CFRPs for the realization of embedded self-sensing systems.

2.2 Research Goal

The goal of this research is to advance the state-of-the-art of EIT damage detection through detecting different damage modes within a 3D, geometrically complex, CFRP prepreg laminate. EIT has been extensively studied with flat CFRP plates, but this work seeks to increase the complexity of laminates investigate while also using prepregs. Namely, the shape of this laminate will represent a simplified general support structure for the demonstration of EIT approaches for damage detection in "real world"-like structures. This geometry includes features with distinct surfaces with different orientations. Additionally, the CFRP's anisotropic conductivity will be characterized and implemented within the mathematical framework to develop techniques that lead towards accurate damage detection. The EIT formulation will be modified as needed to investigate the best approach for effective damage reconstructions via EIT. These efforts aim to progress CFRPs and the EIT damage detecting modality for use in embedded self-sensing systems of the future.

2.3 Thesis Organization

This thesis is organized in the following order. First, the mathematical EIT framework is presented. Second, the manufacturing process used to create the CFRP specimens is discussed. Next, the specific EIT parameters, like the injection scheme, are specified, along with the experimental setup and procedures for the EIT experiments. The fourth chapter contains the damages and ensuing reconstructed images with observational discussions. Finally, a summary, conclusion, and recommended future work bookend the content of this thesis.

3. ELECTRICAL IMPEDANCE TOMOGRAPHY

The objective of EIT is to produce a conductivity distribution for a domain that has been instrumented with electrodes and subjected to a series of current injections. Direct current (DC) is injected into a specified electrode pair and the voltage is measured for the remaining electrode pairs of the domain. This process is repeated until every electrode pair is subjected to a current injection. This process is done both computationally (i.e. the forward problem) and experimentally. Specifically, this work uses difference imaging where the reconstruction represents a conductivity *change* distribution. That is, the final reconstruction image is a conductivity change to the domain relative between an initial "baseline" and "referenced" state. The inverse problem then seeks a conductivity change distribution that minimizes the difference from the experimentally obtained and the computationally calculated voltage data used to predict the conductivity distribution. The forward and inverse problems are described below. Full derivations of these equations can be found in reference [54]. All EIT code was developed in-house and written by the author in MATLAB.

Within the context of self-sensing materials, EIT implies the use of DC currents. Traditionally, interest in EIT research was for biomedical applications, where alternating current (AC) was used. Technically, electrical resistance tomography (ERT) denotes the use of DC current, but the term EIT is often used in structural sensing applications. Therefore, as clarification, this work refers to EIT with the use of DC currents to map the DC conductivity distribution.

3.1 Forward Problem

The forward problem starts with Laplace's equation for steady-state diffusion without internal current sources, as shown in Eq. (3.1). Here, σ_{ij} is the conductivity distribution and u is the domain potential. Einstein summation notation is employed here where repeated indices imply summation through the dimension of the domain.

$$\frac{\partial}{\partial x_i}\sigma_{ij}\frac{\partial u}{\partial x_j} = 0 \tag{3.1}$$

Equation (3.2) enforces the complete electrode model (CEM) boundary conditions to Eq. (3.1), which simulates contact impedance between the perfectly conducting electrodes and the domain. The CEM boundary conditions resolve the contact impedance between the electrodes and domain, incorporate the finite size of real electrodes (as opposed to point electrodes), and provide an additional degree of freedom to the electrode voltage solutions. Here, z_l is the lth electrode contact impedance, n_j is the outward–pointing normal vector to the domain, and V_l is the lth electrode voltage. However, it should be noted that the repeated subscript l does not imply summation unless explicitly stated with the Σ operator. Additionally, Eq. (3.3) imposes conservation of charge within the domain, where the sum of current through the electrodes is zero. Here, L is the total number of electrodes and E_l is the area of the lth electrode. Finally, Eq. (3.4) explicitly imposes that no current passes through portions of the domain that do not include the electrodes. Here, x_i is a position vector within the domain and $\partial\Omega$ is the domain's boundary. The CEM boundary conditions have been widely shown to accurately approximate the current–voltage relationship [55].

$$\sigma_{ij}\frac{\partial u}{\partial x_i}n_j = \frac{1}{z_l}\left(V_l - u\right) \tag{3.2}$$

$$\sum_{l=1}^{L}\int\limits_{E_l}\sigma_{ij}\frac{\partial u}{\partial x_i}n_j \; \mathrm{d}S_l = 0 \tag{3.3}$$

$$\sigma_{ij}\frac{\partial u}{\partial x_i}n_j = 0 \quad \text{on} \quad x_i \in \partial\Omega \setminus \bigcup_{l=1}^{L} E_l \tag{3.4}$$

The forward problem is thus solved by the discretization of the domain via the finite element method (FEM). The forward problem is represented in matrix form via Eq. (3.5). Here, $\boldsymbol{\Phi}$ is the domain potentials vector, $\boldsymbol{V}$ is the electrode voltages vector, and $\boldsymbol{I}$ is the electrode currents vector. The four matrices $\boldsymbol{A}_M$, $\boldsymbol{A}_Z$, $\boldsymbol{A}_W$, $\boldsymbol{A}_D$ that make up the first term on the left-hand side are defined in Eqs. (3.6–3.9). In Eq. (3.6), $A^{e}_{M\ ij}$ represents the local diffusion stiffness matrix where the ith row of the jth column corresponds to the eth element. These local diffusion stiffness matrices are assembled into a global stiffness matrix, $\boldsymbol{A}_M$. Furthermore, Eqs. (3.7–3.9), add a degree of freedom through the relationship between the electrode contact impedances and the domain. Additionally, the w_i terms represent linear interpolation functions for the FEM.

$$\begin{bmatrix} \boldsymbol{A}_M + \boldsymbol{A}_Z & \boldsymbol{A}_W \\ \boldsymbol{A}_W^T & \boldsymbol{A}_D \end{bmatrix} \begin{bmatrix} \boldsymbol{\Phi} \\ \boldsymbol{V} \end{bmatrix} = \begin{bmatrix} \boldsymbol{0} \\ \boldsymbol{I} \end{bmatrix} \tag{3.5}$$

$$A^e_{M\ ij} = \int\limits_{\Omega_e} \frac{\partial w_i}{\partial x_k} \sigma_{kl} \frac{\partial w_j}{\partial x_l} \, \mathrm{d}\Omega_e \tag{3.6}$$

$$A_{Z\ ij} = \sum_{l=1}^{L} \int\limits_{E_l} \frac{1}{z_l} w_i w_j \, \mathrm{d}S_l \tag{3.7}$$

$$A_{W\ li} = -\int\limits_{E_l} \frac{1}{z_l} w_i \, \mathrm{d}S_l \tag{3.8}$$

$$A_D = \mathrm{diag}\left(\frac{E_l}{z_l}\right) \tag{3.9}$$

Finally, Eq. (3.5) is only solvable to an arbitrary constant. Therefore, it is physically convenient to enforce electrical potential of the *negative* electrode from the injection electrode–pair to zero. The additive shift is also reflected in the domain solution. Performing this electric potential shift helps reinforce the physics of conducting current injections into a domain, however, computationally the effect is largely negated because difference imaging was employed. In this work, a three-dimensional mesh using linear tetrahedrons were used. The first two solutions of the forward problem are seen in Fig. (3.1). A domain potential is predicted by the forward model for each current injection conducted on the domain. Figure (3.1a) depicts the domain solution from the first injection pair, while Fig. (3.1b) shows the subsequent domain solution from the next injection pair.

3.2 Inverse Problem

The EIT inverse problem seeks to minimize the error between the experimental and model predicted voltages. However, the inverse problem is ill-posed and requires some additional information to produce meaningful reconstructions in the form of a regularization term to

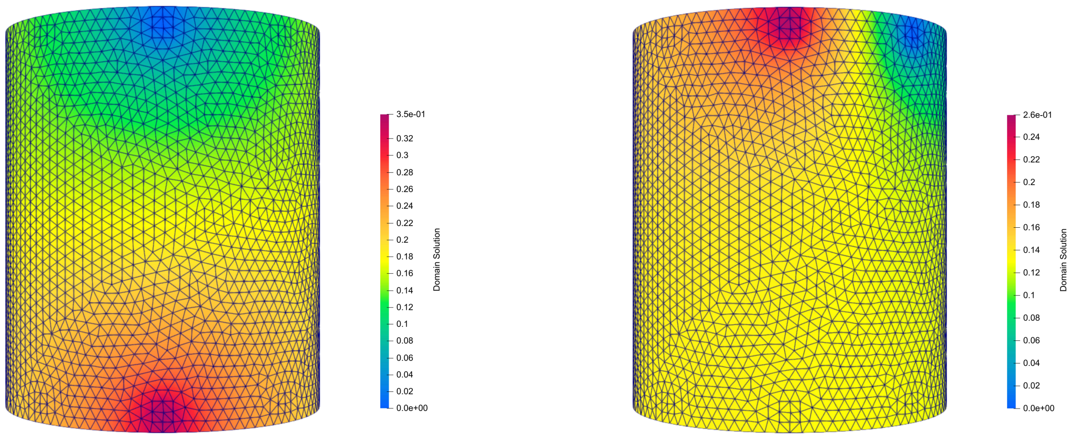

(a) (b)

Figure 3.1. (a) Current injected and grounded into the first electrode pair.(b) Current injected and grounded into the second electrode pair.

constrain the solution space. Several approaches to the error minimization and regularization algorithms have been proposed with suggested use-cases [56–59]. In this work, two formulations for the error minimization were conducted. The first approach was a ℓ_2-norm least-squares error minimization, and the second was a ℓ_1-norm error minimization using a primal-dual interior point method (PDIPM). Note that the PDIPM algorithm was not developed for this work and was used as a secondary comparative tool against the traditionally used ℓ_2-norm minimization. The PDIPM algorithm was derived from references [60, 61]. The regularization was formulated as a minimization in the least-squares sense for both error minimization approaches. Applying the ℓ_2-norm for regularization uses the discrete Laplacian operator and favors smoothly varying solutions while adding resilience against oscillatory noise.

3.3 General Formulation for Difference Imaging Inverse Problem

In general, the EIT inverse problems seeks a conductivity distribution; however, the inverse problem is also severely ill-posed and underdetermined with sensitivity to outlier data and noise. To this end, a minimization is performed on the differences between the experimentally collected inter-electrode voltage differences and the computationally predicted values. Sources like experimental errors, electrode placement, and differences between the computational and actual physical domains contribute to these sensitivities when solving the inverse problem. A method to counteract these obstacles is through difference imaging, where these error sources largely subtract out. Therefore, the general minimization for the EIT inverse problem is formulated in Eqn. (3.10). Here, $\delta\boldsymbol{\sigma}$ is a vector of conductivity values (scalars or tensors depending on whether an isotropic or anisotropic formulation is used; see Section (3.6)), that correspond to the change in the conductivity distribution of each element within the mesh from the forward problem. Then, $\delta\boldsymbol{\sigma}^*$ is the change in conductivity distribution that satisfies the error minimization between the experimental data and the computational solution. The first term is the error minimization term, which is generalized to be m^{th} norm raised to the m^{th} power. It is reiterated that the EIT formulation is ill-posed and requires regularization to help constrain the solution. The second term is the regularization term, where $\boldsymbol{R}$ is a generalized regularization variable, of which there are multiple mathematical approaches done for the EIT problem. This regularization term is specified to be the ℓ_2-norm raised to the 2^{nd} power and therefore uses the discrete Laplace operator. Additionally, α is a scalar hyperparameter dictating the degree of regularization.

$$\delta\boldsymbol{\sigma}^* = \underset{\delta\sigma}{\arg\min} \left\| \boldsymbol{V_m} - \boldsymbol{W} \right\|_m^m + \alpha \left\| \boldsymbol{R}\left(\delta\boldsymbol{\sigma}\right) \right\|_n^n \tag{3.10}$$

In difference imaging, the domain is inspected at two different times or states, i.e. $\boldsymbol{V}(t_1)$ and $\boldsymbol{V}(t_2)$. Typically the first state is an undamaged or *baseline* state, followed by a second damaged state. However, any two different states can be used in EIT. Experimental data collected at both of these states reduce the previously mentioned negative effects, which improves the quality of the reconstructed conductivity distribution. Equation (3.11) shows the difference of these two voltage data sets, defined as $\boldsymbol{V_m}$. A similar vector of difference voltages is supplied via the forward problem, defined in Eqn. (3.12) as $\boldsymbol{W}$. Here $\delta\boldsymbol{\sigma}$ is the conductivity difference from the undamaged and damaged states and $\boldsymbol{F}(\cdot)$ is the operator for the forward problem evaluated at each state. The $\delta\boldsymbol{\sigma}$ term can be isolated from $\boldsymbol{F}(\boldsymbol{\sigma}+\delta\boldsymbol{\sigma})$ through a truncated Taylor series expansion centered about the initial estimate for the conductivity, as seen in Eq. (3.13). We then define the sensitivity matrix as $\boldsymbol{J} = {}^{\partial \boldsymbol{F}(\boldsymbol{\sigma_0})}/_{\partial \boldsymbol{\sigma}}$. Consequently, $\boldsymbol{W}$ can be represented as shown in Eq. (3.14).

$$\boldsymbol{V_m} = \boldsymbol{V}(t_2) - \boldsymbol{V}(t_1) \tag{3.11}$$

$$\boldsymbol{W} = \boldsymbol{F}(\boldsymbol{\sigma}+\delta\boldsymbol{\sigma}) - \boldsymbol{F}(\boldsymbol{\sigma_0}) \tag{3.12}$$

$$\boldsymbol{F}(\boldsymbol{\sigma}+\delta\boldsymbol{\sigma}) \approx \boldsymbol{F}(\boldsymbol{\sigma_0}) + \frac{\partial \boldsymbol{F}(\boldsymbol{\sigma_0})}{\partial \boldsymbol{\sigma}}\delta\boldsymbol{\sigma} \tag{3.13}$$

$$\boldsymbol{W} = \boldsymbol{J}\delta\boldsymbol{\sigma} \tag{3.14}$$

3.4 Error Minimization: ℓ_2-norm

In the case where $m = 2$ in Eqn. (3.10), the square of the ℓ_2-norm is specified for both the error and regularization terms. This approach can be solved in a one-step minimization. An explicit closed-form of Eqn. (3.10) can be found by expanding both of the squared norm terms, taking the gradient with respect to $\delta\boldsymbol{\sigma}$, setting the equation to zero and isolating $\delta\boldsymbol{\sigma}$. Therefore, Eqn. (3.15) solves the objective function minimization in a least-squares sense. Additionally, the objective function can be represented in an augmented matrix form, as seen in Eqn. (3.16), which is a form compatible with many numerical solvers like MATLAB's LSQLIN function, which is a constrained linear least-squares algorithm. The solution can be constrained by assumptions on the solution. The lower bound is set so the conductivity loss cannot exceed the baseline estimate. Additionally, there should not be a conductivity increase from damage, but a small allowance over the initial estimate is set to account for experimental data noise.

The regularization term has been replaced with the discrete approximation of the Laplace operator, $\boldsymbol{L}$. The advantage of the Laplace operator is that highly oscillatory conductivity changes are filtered to minimizes the effects of outlier noise data with favoring smoothly varying solutions. The discrete Laplace operator is defined in Eqn. (3.17). Here, $\boldsymbol{L}_{ij}$ represents a square symmetric matrix equal in size to the number of elements in the mesh. The Laplacian matrix is assembled by determining the number of elements adjacent to a specific element. In three-dimensional space, an adjacent element is defined as sharing a *face* or having the same three nodes as another element. Since the mesh is comprised of tetrahedrons, the max number of shared faces can be four. If the ith element shares a face with the jth element, a value of -1 is added at the i, j index. The ith diagonal index of $\boldsymbol{L}$ is the absolute sum along the ith row and represents the *degree* of connectedness of the ith element.

$$\delta\boldsymbol{\sigma}^* = \left(\boldsymbol{J}^T\boldsymbol{J} + \alpha\boldsymbol{L}^T\boldsymbol{L}\right)^{-1}\boldsymbol{V}_m^T\boldsymbol{J} \tag{3.15}$$

$$\delta\boldsymbol{\sigma}^* = \min_{\delta\sigma}\left\|\begin{bmatrix}\boldsymbol{J}\\ \alpha\boldsymbol{L}\end{bmatrix}\delta\boldsymbol{\sigma} - \begin{bmatrix}\boldsymbol{V_m}\\ \boldsymbol{0}\end{bmatrix}\right\|_2^2 \tag{3.16}$$

$$\boldsymbol{L} = L_{ij} = \begin{cases}\text{degree}(\Omega_e) & \text{if } i = j\\ -1 & \text{if } i \neq j \text{ and } \Omega_e \text{ is adjacent to } \Omega_i\\ 0 & \text{otherwise}\end{cases} \tag{3.17}$$

3.5 Error Minimization: ℓ_1-norm

The PDIPM approach solves Eqn. (3.10) using the ℓ_1-norm of the error term, $m = 1$, and reformulates the inverse problem by the addition of a second objective function that is solved simultaneously. The PDIPM algorithm is presented in Eqs. (3.18 – 3.19), where $\boldsymbol{W}$ is expanded for clarity. Again, this approach was not developed specifically by this work and instead was used as a tool for characterizing the difference in error minimization approaches that resulted in the best EIT reconstruction images. Use of the ℓ_1-norm is especially important for limiting the effect of outlier data, which the ℓ_2-norm is sensitive to.

For the sake of clarity, within the formulation of PDIPM, $\delta\boldsymbol{\sigma}$ is redefined as $\boldsymbol{x}$ because the PDIPM is an iterative algorithm. That is, using $\boldsymbol{x}$ prevents the use of cumbersome $\delta\left(\delta\boldsymbol{\sigma}\right)$ notation.

$$\boldsymbol{x}^{*} = \min_{x} \left\| \boldsymbol{Jx} - \boldsymbol{V_m} \right\|_1^1 + \alpha \left\| \boldsymbol{Lx} \right\|_2^2 \tag{3.18}$$

$$\boldsymbol{z}^{*} = \max_{z} \begin{cases} \boldsymbol{z}^T \left(\boldsymbol{Jx} - \boldsymbol{V}_m \right) + \alpha \left\| \boldsymbol{Lx} \right\|_2^2 & : \ |z_i| \leq 1 \\ \boldsymbol{J}^T \boldsymbol{z} + \alpha \boldsymbol{L}^T \boldsymbol{Lx} = 0 \end{cases} \tag{3.19}$$

In the above equations, x is the primal problem and z is the dual problem. Both are found iteratively such that $x^{n+1} = x + \delta x$ and $z^{n+1} = z^n + \min(1, \lambda)\delta z$ where λ is selected such that $\lambda = \sup(\lambda\colon\ |z_i^n + \lambda\delta z| \leq 1)$ for the $n+1$ iteration by solving the system of equations shown in Eqn. (3.20). The terms $\boldsymbol{E}$ and $\boldsymbol{G}$ are shown in Eqs. (3.21 – 3.22), where $\left(\boldsymbol{Jx} - \boldsymbol{V}_m\right)_i$ is the ith value of the error vector, ε, and z_i is the ith value of the dual vector. β is a small scalar value used to ensure differentiability.

$$\begin{bmatrix} 2\alpha \boldsymbol{L}^T \boldsymbol{L} & \boldsymbol{J} \\ \boldsymbol{GJ} & -\boldsymbol{E} \end{bmatrix} \begin{bmatrix} \delta \boldsymbol{x} \\ \delta \boldsymbol{z} \end{bmatrix} = \begin{bmatrix} \boldsymbol{J}^T \boldsymbol{z} + 2\alpha \boldsymbol{L}^T \boldsymbol{Lx} \\ \left(\boldsymbol{Jx} - \boldsymbol{V}_m \right) - \boldsymbol{Ez} \end{bmatrix} \tag{3.20}$$

$$\boldsymbol{E} = \operatorname{diag}\left(\left(\left(\boldsymbol{Jx} - \boldsymbol{V}_m \right)_i^2 + \beta \right)^{\frac{1}{2}} \right) \tag{3.21}$$

$$\boldsymbol{G} = \operatorname{diag}\left(1 - \frac{\boldsymbol{z}_i \left(\boldsymbol{Jx} - \boldsymbol{V}_m \right)}{\left(\left(\boldsymbol{Jx} - \boldsymbol{V}_m \right)_i^2 + \beta \right)^{\frac{1}{2}}} \right) \tag{3.22}$$

3.6 Anisotropic Formulation

The previous mathematical framework presented was for a generalized case assuming electrical isotropy. This framework is not appropriate for materials with anisotropic conductivity like CFRPs and requires changes to the EIT formulation. Instead of a vector of scalar values defining the conductivity distribution, the anisotropic formulation requires a vector of *tensors* defining the conductivity distribution. EIT is already an ill-posed, underdetermined inverse problem, resulting in no unique solution. Seeking the solution that satisfies the minimization becomes more difficult because there are now six unknowns, σ_{ij} is a symmetric 2^{nd}-order tensor, instead of one in the isotropic case. One method of overcoming this obstacle is to transform the problem with a scalar multiple of the conductivity tensor such that the eigenvectors are maintained [62, 63]. The conductivity tensor can then be rewritten as $\sigma_{ij} = \kappa\bar{\sigma}_{ij}$, where κ is the multiplicative factor chosen so that $\det|\bar{\sigma}_{ij}| = 1$. Implementing this change back to the EIT formulation requires the sensitivity matrix to be redefined as $\boldsymbol{J}^{\boldsymbol{\kappa}} = {}^{\partial(\boldsymbol{\kappa}\bar{\boldsymbol{\sigma}}_{ij})}/_{\partial\boldsymbol{\kappa}}$. The terms $\boldsymbol{\kappa}$ and $\bar{\boldsymbol{\sigma}}_{ij}$ are now boldfaced to indicate vectorization for use in the finite element method. The new objective function now seeks the scalar distribution change, $\delta\boldsymbol{\kappa}$, that satisfies the minimization and is shown in augmented matrix form in Eqn. (3.23). To constrain the solution space for the minimization, assumptions about the piezoresistive behavior from damage are enforced. Conductivity loss cannot be greater than 100% of the baseline, meaning the lower limit is bounded by $-\kappa$. In the experimental EIT data, there will be variation in the measured voltage data and an allowance for that variation bounds the upper limit at 1% of the baseline.

$$\delta\boldsymbol{\kappa}^* = \min_{-\kappa \,\leq\, \delta\kappa \,\leq\, .01\kappa} \left\| \begin{bmatrix} \boldsymbol{J}^{\boldsymbol{\kappa}} \\ \alpha\boldsymbol{L} \end{bmatrix} \delta\boldsymbol{\kappa} - \begin{bmatrix} \boldsymbol{V}_m \\ \boldsymbol{0} \end{bmatrix} \right\|_2^2 \tag{3.23}$$

The explicit form of the sensitivity matrix, $\boldsymbol{J}^{\boldsymbol{\kappa}}$, can be seen in Eqn. (3.24). The sensitivity matrix is the integral of the dot product of the gradient of the voltage on the eth element due to the current supplied to the Mth electrode injection pair and the gradient of the voltage on the eth element due to the Nth adjoint field, where the adjoint field is the domain solution due to a unit current injection supplied to the Nth electrode pair. Here, MN is a single index and the integral is evaluated over the eth element. A physical interpretation of $\boldsymbol{J}^{\boldsymbol{\kappa}}$ is the sensitivity of the Nth electrode pair due to conductivity perturbations of the eth element from the current injected in the Mth electrode pair. An in-depth derivation of the Jacobian can be found in [19, 48].

$$\boldsymbol{J}^{\boldsymbol{\kappa}}_{MN\ e} = -\int_{\Omega_e} \frac{\partial u^M}{\partial x_i} \bar{\sigma}^e_{ij} \frac{\partial \bar{u}^N}{\partial x_i}\, \mathrm{d}\Omega_e \tag{3.24}$$

The isotropic formulation of $\boldsymbol{J}$ is a simplification of Eqn. (3.24). In the isotropic case, the normalized conductivity tensor, $\bar{\boldsymbol{\sigma}}_{ij}$, is replaced with the Kronecker delta, $\boldsymbol{\delta}_{ij}$. The isotropic formulation for $\boldsymbol{J}$ is shown in Equation (3.25) below.

$$\boldsymbol{J}_{MN\ e} = -\int\limits_{\Omega_e} \frac{\partial u^M}{\partial x_i} \frac{\partial \bar{u}^N}{\partial x_i} \, \mathrm{d}\Omega_e \tag{3.25}$$

3.7 Conductivity Tensor Transformation

The geometry used in this work requires the element-wise conductivity tensor, σ^e_{ij}, to undergo a tensor transformation. Chapter (4) contains in-depth detail about the geometry used in this work, but will be briefly described here. As previously mentioned, a mesh using tetrahedral elements is used to discretize the domain of interest. The domain of interest is a cylindrical shell shape with an inner annulus. The generation of this mesh has a defined global coordinate reference frame with the x_3-axis aligned with the centerline of the cylinder. Because this work involves a non-planar geometry, the same conductivity tensor cannot be applied to every element. The element-wise conductivity tensor must be transformed into the global coordinate reference frame for the forward problem to be calculated correctly. The EIT the formulation already involves element-wise calculations, requiring no modifications. Therefore, the only additional task is to transform the conductivity tensor for each element in the mesh into the global coordinate reference frame.

Figure (3.2) shows the global coordinate reference frame and an arbitrary elemental coordinate reference frame of the mesh. The elemental coordinate reference frame is chosen to enforce the through-thickness direction on the shell is always in the x'_1 direction. Therefore, only a two-dimensional rotation about the x_3-axis is required for the transformation. The position vector, $\boldsymbol{r}$, begins at the global origin to the location of the elemental centroid. The angle, θ, is the angle between $\boldsymbol{r}$ and the global x_1-axis. Equation (3.26) shows the elemental conductivity tensor, Eqn. (3.27) shows the direction cosine rotation matrix, and Eqn. (3.28) shows the equation to perform the tensor transformation.

It is noted here that there are two distinct regions of the geometry will have two different elemental conductivity tensors. The reason for the transformation described in the previous paragraph was to enforce the through-thickness direction based on the domain's geometry. The through-thickness direction of the annulus region needs to be enforced as well, which is in the x_3 direction. Physically speaking, the shell begins where the planar surface of the annulus ends and denotes the location where the different conductivity tensors are applied. Mathematically speaking, if the magnitude of $\boldsymbol{r}$ is longer than the radius of the annulus, i.e. $|\boldsymbol{r}| > r_{\text{annulus}}$, the elemental shell conductivity tensor is applied. These two tensors are described more in Section (5.6).

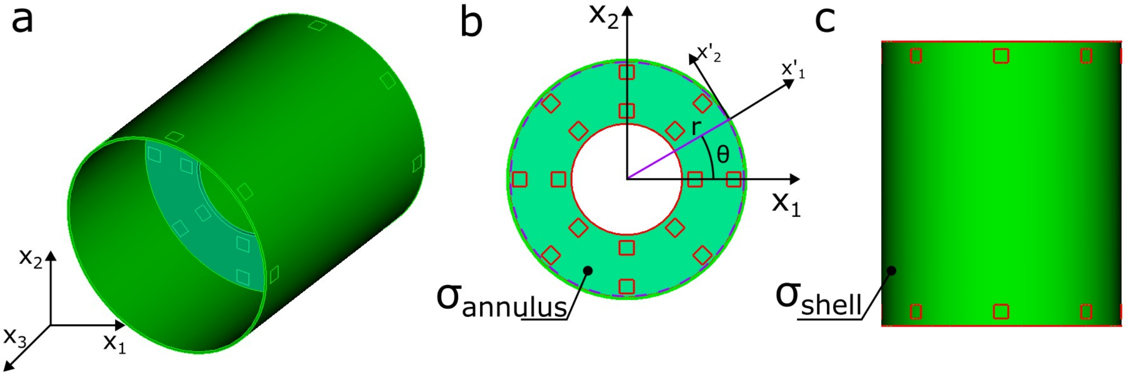

Figure 3.2. a) Isometric view, b) top view showing region of σ_{annulus}, c) side view showing region of σ_{shell}.

$$\sigma_{ij}^{e} = \begin{bmatrix} \sigma_1 & 0 & 0 \\ 0 & \sigma_2 & 0 \\ 0 & 0 & \sigma_3 \end{bmatrix} \tag{3.26}$$

$$R = \begin{bmatrix} \cos\theta & -\sin\theta & 0 \\ \sin\theta & \cos\theta & 0 \\ 0 & 0 & 1 \end{bmatrix} \tag{3.27}$$

$$\sigma_{ij}^{e\,\prime} = [R][\sigma_{ij}^{e}][R]^{T} \tag{3.28}$$

4. MANUFACTURING

This chapter describes the manufacturing of two types of CFRP laminates used in this work. The first section presents the laminate used for EIT experiments and the associated development work. Next, the process used to produce conductivity test measurements is described.

4.1 Research Specimen: The Shell-Annulus

The specimen geometry designed for EIT experiments consists of a outer cylindrical shell with an internal annulus about the mid-plane, and is given the Shell-Annulus (SA) nomenclature. Two different applications of composites motivated the geometry of the SA. The first was to have a CFRP laminate that could be a plausible facsimile of a support structure. Thin-walled structures are used extensively for aerospace structural supports due to their high strength-to-weight ratios and were a primary source of inspiration for the geometry. The second application is the use of composites as sacrificial impact energy attenuator structures, which are often tube shaped. Research has increased investigating these sacrificial structures as crash boxes for the automotive racing industry and protecting civil structures, as seen in [64–67]. However, there was no specified loading scenario dictating aspects the geometry or the laminate sequence to maintain the geometry's generality.

The layup sequence is defined as $[(0^\circ/90^\circ)_2/\pm45^\circ_2]_S$, and is an eight–ply, balanced, symmetric, and mechanically quasi-isotropic laminate. Both the shell and annulus portions of the laminate follow the same layup sequence. This layup was chosen because it would provide dimensionally stability from the curing process. The material system used was a 3K 2×2 twill weave carbon fiber prepreg purchased from FibreGlast (Brookville, OH, USA). This material was selected for several reasons. The first reason was to use the kinds of materials currently used in aerospace, where prepreg carbon fiber is used instead of dry fabrics. Also, this specific prepreg did not require freezer storage and had a shelf-life of six months. Finally, the prepreg was curable without an autoclave. This allowed all CFRP manufacturing to be completed in-house with available laboratory equipment.

The SA specimen had the following nominal dimensions. The annulus had a nominal outer diameter (O.D.) of 4.25 (in.) and the inner diameter was 2.0 (in.). The thickness of both the shell and annulus was 0.96 (in.). The O.D. of the shell was 4.42 (in.) and the height was 5.0 (in.). A graphical representation of the SA geometry is shown in Fig. (4.1).

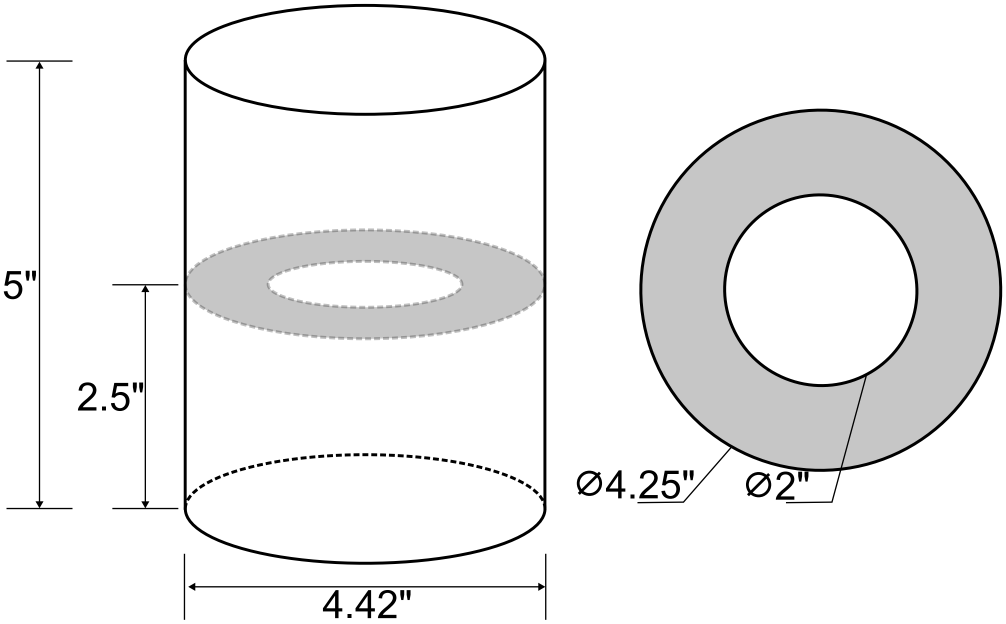

Figure 4.1. Shell-Annulus (SA) nominal geometric representation with annulus excerpt.

As previously stated, the SA specimen was manufactured in-house and required significant development to the manufacturing process. The expertise of this research group is not composite manufacturing, however best efforts were done to produce geometrically complex CFRP laminates with acceptable results. The main challenge was how to join the shell and annulus portions together into one monolithic structure. It was decided both parts of the laminate would be made and joined in the same cure as opposed to performing a secondary cure to join two separate laminates. The primary driver for this decision was concern of a conductive *dead zone* where the two laminates meet. An equal concern was having dimensional mismatch between two laminates making it impossible to be joined smoothly. Therefore, the construction of the entire laminate occurred in one layup process and required the design of tooling to facilitate manufacturing.

The process to join the shell and annulus portions of the laminate was to have portions of the annulus plies overlap plies of the shell. In effect, the shell and annulus would be electrically connected through these overlapped contact areas. A cross-section of this approach is seen in Fig. (4.2). Plies from both the top and bottom half of the annulus were cut in a way to accommodate a 90° bend to be draped along the shell plies.

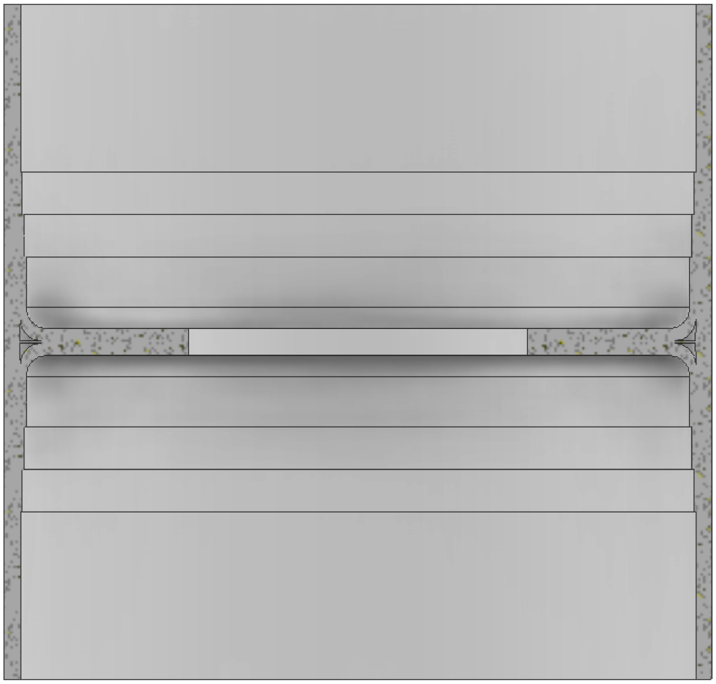

Figure 4.2. SA cross–section showing ply overlaps (Not to scale.).

4.1.1 Acrylic Templates

Prepreg cutting templates were designed to consistently shape cut plies for the laminate. Multiple templates were designed and manufactured from acrylic using a Trotec Flexx 400 laser cutter located at Purdue's Bechtel Innovation Design Center. These templates also had alignment features to help cut the prepreg with the correct orientations (i.e. ±45° and 0°/90°). The efficiency of cutting the plies was also increased through use of the templates. The templates used and can be seen in Fig. (4.3). The annulus required two separate templates because the two innermost plies would not be draped onto the shell. The rationale was to minimize the void at the corner with a small number of plies. Therefore, a 4.25 (in.) diameter template and a 6 (in.) diameter template were used to cut the annulus plies with a utility knife. The lengths of these draping cutouts were sized so that there was still a uniform 4.25 (in.) diameter coverage on the annulus. A rectangular template was used to quickly cut plies for the shell portion. Several small rectangular cutouts were also implemented into the templates to support prepreg alignment during cutting.

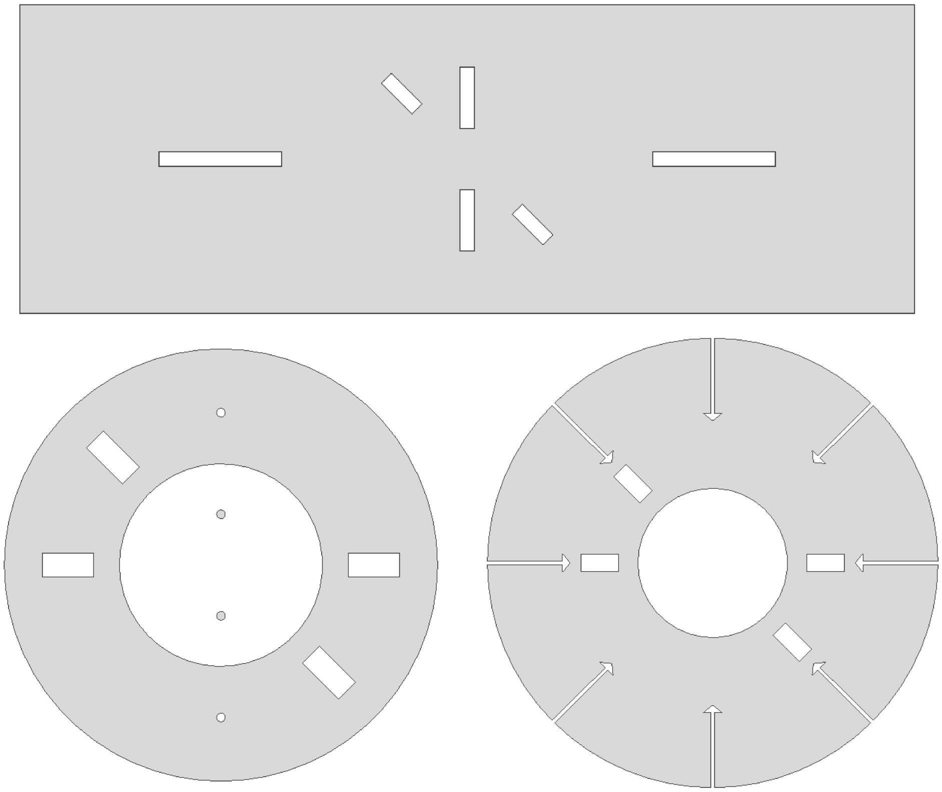

Figure 4.3. CFRP prepreg acrylic cutting templates; shell (top), 4.25 (in.) annulus (bottom left), and 6 (in.) annulus (bottom right) (Not to scale.).

4.1.2 Foam Core Molds

High-temperature polyisocyanurate (PIR) (ITW/Grainger) foam was used as a sacrificial foam core to fill the empty internal space of the SA specimen during the layup process. The foam core was required so the laminate had a mold for shaping and to facilitate bonding of the shell and annulus portions during the vacuum curing process. After curing, the foam molds were chiseled out. PIR foam had a compatible working temperature to withstand the curing temperature of the CFRP prepreg. More commonly available foams, like polyurethane and polystyrene, did not meet this requirement.

Two inner foam molds were designed to have a layup process where the annulus portion can be constructed and pre-shaped for the shell plies to wrap around the molds. Figure (4.4) show a graphical representative of the two molds integrated with the full laminate. The foam was only available with a 1 (in.) thickness so multiple pieces of foam were stacked to produce a height of 3 (in.). The stack was secured with toothpicks because using an adhesive would make removing the foam more difficult. It was key for the foam to be cut as perfectly as possible since the laminate would form to the surface of the molds. An aluminum 6061-T6 tube with an inner diameter of 4.25 (in.) (McMaster-Carr, 9056K991) was used as a stamp die cutting tool, Fig. (4.5).

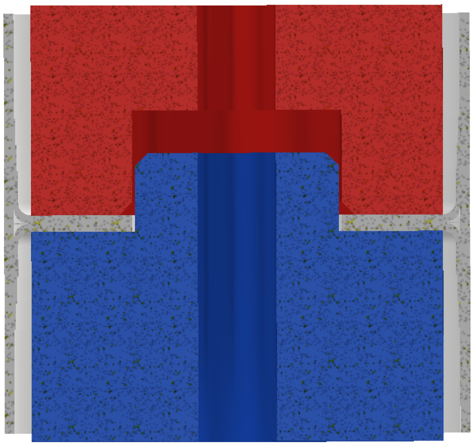

Figure 4.4. Graphical representation of foam core molds within the SA specimen.

To help facilitate foam removal, the exposed edges of the foam were covered with an adhesive backed low–friction Flourinated Ethylene Propylene (FEP) film (McMaster-Carr, 5805T11). Once again, a film was selected with an operating temperature above the prepreg curing temperature. The film acted as a barrier between the resin and the foam so the foam would not bond to the laminate. An unexpected consequence of the PIR foam was it's tendency to easily flake dust from very light abrasions. Once the film was applied to

Figure 4.5. Al6061-T6 die cutting tool and resulting PIR foam mold pieces

the foam and cleaned of dust, the foam could be handled without producing more dust to protect the laminate from foam debris during layup.

4.1.3 Layup Process

The layup and vacuum bagging approach followed processes common with manufacturing CFRP laminates. Figure (4.6) shows a diagram of the layup materials sequence. The inner foam molds were already described in the previous section and the materials on the outer surface of the SA laminate was a layer of peel-ply, then release film, and finally a breather cloth. The annulus was constructed in halves before being physically joined. Then the shell plies could be wrapped around the molds.

Multiple debulk steps were required throughout the layup process to prevent wrinkles and bunching of the plies. The debulking ensured the plies conformed to the molds and also prevented ply shifting as the layer count increased. Once the first ply was place on the foam mold, ply was placed under vacuum for at least 15 minutes at room temperature and then removed from vacuum. Next, after every two subsequent plies, the partial laminate was debulked again under the same conditions. After each debulk, the laminate was inspected for wrinkling and adjusted as required. Figure (4.7) shows one half of the partial annulus laminate and both halves under a debulk. Peel-ply was used during these steps to assist in removal of the parts from the vacuum bag. Additionally, care was taken to ensure the vacuum bag did not snag on corners of the geometry or pull on the plies. This process continued until both halves were ready to be joined. Once joined, another debulk was performed. Then the plies for the shell were placed onto the foam molds. The same debulk process was completed until the layup sequence was complete. The laminate was then cured in an oven at 290 °F for two hours per the manufacturer's instructions. Two SA specimens were manufactured using these steps and Fig. (4.8) shows the SA specimen after being removed from the vacuum bag and after the foam was removed.

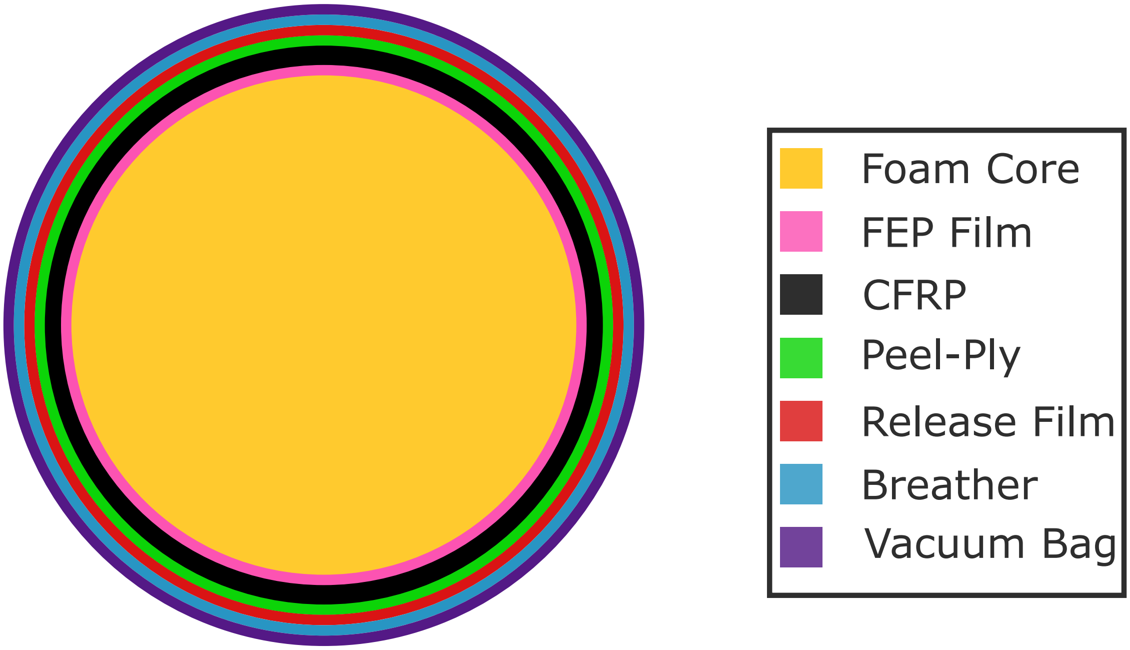

Figure 4.6. Vacuum bag materials diagram.

4.1.4 Electrode Integration

The SA specimen was instrumented with 32 surface mounted electrodes. The distribution of electrodes can be viewed as four rings of eight electrodes. These rings are comprised of the top/bottom of the shell and the inner/outer edges of the annulus. All electrodes were designed to be .25 × .25 (in.) squares and to be aligned vertically and concentrically, resulting in a precisely distributed electrode array. To support this goal, paperboard (McMaster-Carr,

Figure 4.7. CFRP annulus laminate halves layup under debulk.

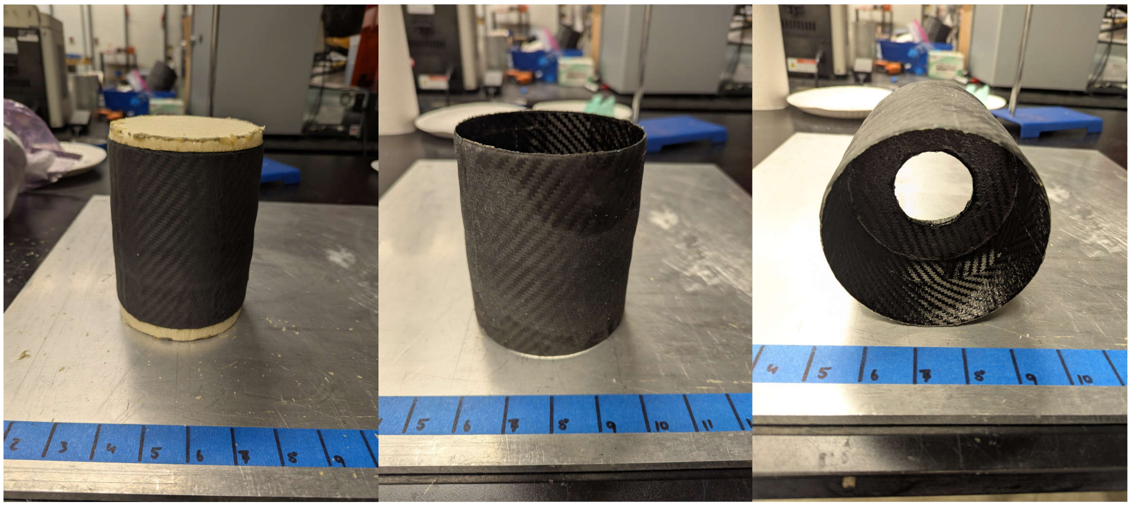

Figure 4.8. SA specimen after curing with inner foam mold (left) and with the foam removed: side view (middle) and top view (right).

3659N11) electrode templates were made for the exact placement and sizing of electrodes. Figure (4.9) shows the electrode templates being cut for shell and annulus electrodes. The templates were first used to mark locations on the specimen that require sanding. Sanding removes the outer epoxy layer to expose carbon fibers before the electrodes are attached. A wet-sanding process using 600 grit sandpaper, followed by a 1200 grit sandpaper, was performed at all electrode locations and cleaned with acetone. To have clean electrode edges, masking tape was used over the templates to cut out electrode squares and affixed to the specimen. The masking tape was finely adjusted for electrode alignment as required. Each electrode was then given two coats of conductive silver paint from Ted Pella Inc. (Redding, CA, USA), allowing dry time after each coat. Finally, the electrode dimensions were measured and shown in Fig. (4.10). COTS right–angled jumper wire pins were attached to each painted electrode using silver conductive epoxy H20E EPO-Tek, also from Ted Pella Inc. High heat epoxy putty from J-B Weld (Marietta, Ga, USA), was used to assist in the placement of the pins and provide additional structural reinforcement. The SA laminate was then placed in an oven at 176 °F for 1.5 hours to cure the conductive epoxy. Figure (4.11) shows the final configuration of electrodes with pins.

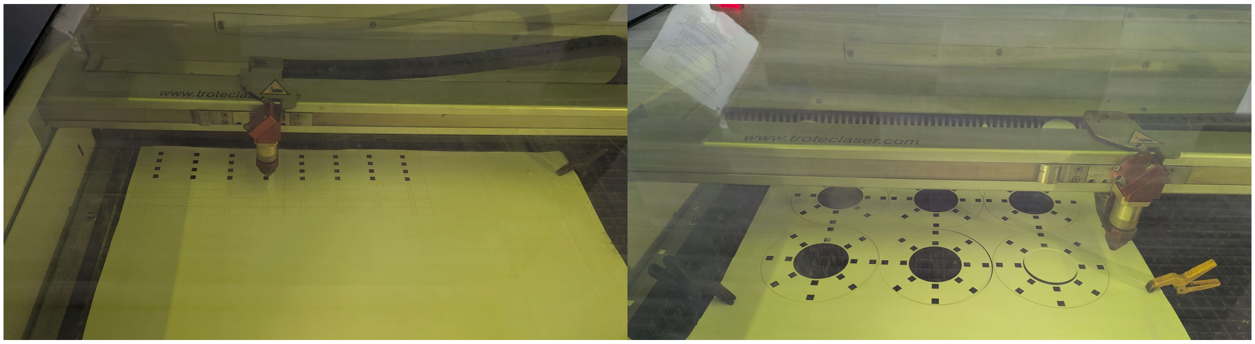

Figure 4.9. Laser cutting of electrode paper templates; shell (left), annulus (right).

Figure 4.10. Electrode dimension measurements for shell: length and width and annulus electrodes.

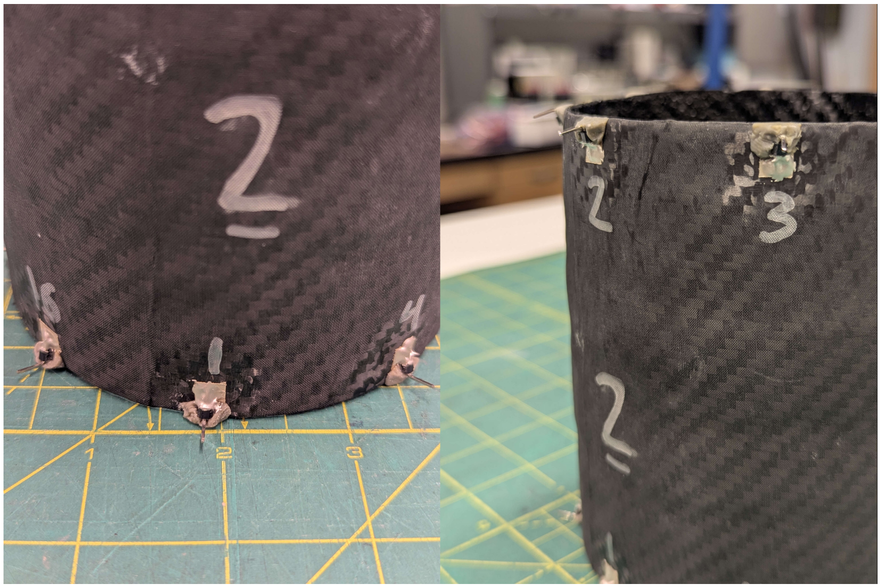

Figure 4.11. Shell electrodes with pins attached.

4.2 Conductivity Specimen: Square Plate

A flat plate laminate was made to cut out planar specimens for conductivity measurements of the material. The layup sequence mimicked that of the SA specimen, albeit with a larger thickness to make instrumenting edge-mounted electrodes easier. The layup sequence is defined as $[(0^\circ/90^\circ)_2/\pm 45^\circ_2]_{2S}$, and is the same as the SA specimen but repeated at the laminate's mid-plane. A flat CFRP plate measuring approximately 9 × 9 × .14 (in.) was manufactured using the hand layup vacuum bag process and cured in an oven at 290 °F for two hours. The laminate was laid against an aluminum plate pretreated with two coats of FibreGlast's 1153 FibRelease mold release. Peel-ply was placed on top of the final top layer, followed by release film, then a breather cloth. The laminate was then sealed within a vacuum bag.

The nominal test specimen geometry was designed to be 1 × 1 × .14 (in.) (l×w×t). A total of 64 specimens were cut from the flat plate using a wet tile cutting saw, but only 15 were used for conductivity measurements. Because CFRPs have conductive anisotropy, measurements were taken in the three principle directions from the laminate. The planar x_1

and x_2 directions following the fiber orientations and x_3 was the through-thickness direction, where x_1 and x_2 were chosen arbitrarily. The plate laminate and an instrumented specimen for each measurement can be seen in Fig. (4.12). Two coats of conductive silver paint were applied to the two faces perpendicular to the measurement direction of interest. Once again, COTS jumper pins were affixed to each electrode surface for a contact point to the power supply. Silver conductive epoxy H20E EPO-Tek and JB Weld epoxy were used to attach and support the pins. The specimens were then placed in an oven at 176 °F for 1.5 hours to cure the epoxy.

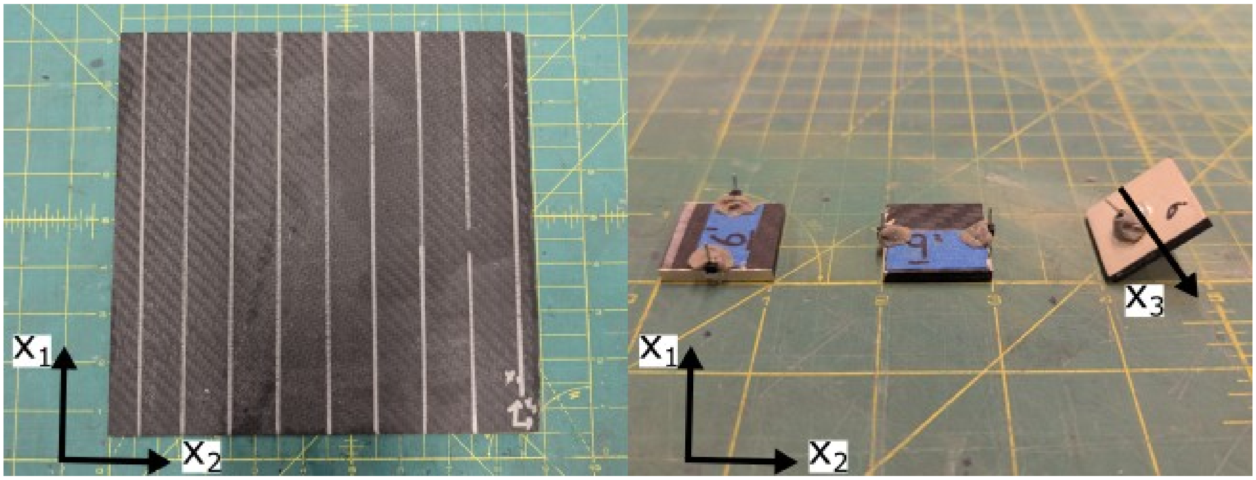

Figure 4.12. a) CFRP plate laminate, (b) Conductivity specimen with conductive silver paint and electrodes attached in the x_1 direction, x_2 direction and x_3 direction.

5. EXPERIMENTAL PROCEDURE

This chapter describes the experimental setup and procedures used in this work. First the injection schemes used in this work are described. Next the conductivity measurement experiment and results are discussed. Finally, the impact test setup used for this work is presented.

5.1 EIT Injection Scheme Motivation

An injection scheme is used to define the order for injecting and grounding electrodes, as well as the inter-electrode voltage differences. This information is important to ensure the EIT formulation is setup properly to match the experiment. As previously seen, the SA specimen was instrumented with 32 surface-mounted electrodes. A total of 16 electrodes were placed on both the shell and annulus regions. The geometry's domain was created and meshed using Corefoam Cubit, a finite element meshing software originally developed by Sandia National Laboratories and commercialized for public use. A total of 25,093 elements were used for this geometry.

A well-known EIT injection scheme is called the *adjacent* scheme. The name refers to the fact that after a current injection is performed, the next neighboring electrode receives a current injection. The pattern repeats until all electrodes have received a current injection. Other injection schemes exist, but the adjacent scheme is commonly seen in the EIT literature because it produces acceptable results. This framework inspired the selection of injection patterns used for this work. The extensive exploration, in-depth characterization, and optimization of injections schemes is outside of the scope of this work. Therefore, any injection scheme that produced reasonable results were acceptable.

5.2 Zigzag Injection Scheme

In the *zigzag* injection scheme, the surface electrode numbering can be seen in Fig. (5.1). The injection of electrodes starts at electrode one and continues sequentially until ending at electrode 32, as seen in the two-dimension projection in Fig. (5.2). The electrode numbering was done in a way such that the injections follow a "zigzag" path along the shell. This specific numbering also avoids modifying the EIT formulation from a traditional adjacent injection scheme. Additionally, this pattern had previous success with EIT damage detection using surface mounted electrodes in a CFRP airfoil [48].

Figures (5.3–5.4) show the first and second current injection pairs and a few representative inter-electrode voltage differences respectively. Not all inter-electrode differences are shown for clarity. An electrode pair is supplied a DC current and the electrode pairs not involved with the current injection are used for inter-electrode voltage differences. Inter-electrode voltage differences physically associated with any injection pair electrode are not used because contact impedance and measurement noise can negatively affect the EIT reconstructions. These voltages are used to assemble $\boldsymbol{V}_m$ and calculated offline as an input into the EIT formulation.

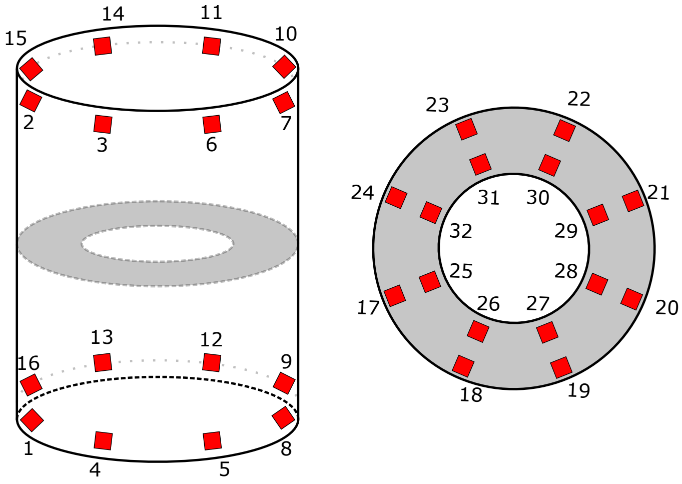

Figure 5.1. Zigzag electrode numbering.

5.3 Isolated Adjacent Injection Scheme

In the *isolated adjacent* injection scheme, the surface electrode numbering can be seen in Fig. (5.5). In this case, each row of electrodes is considered individually, as seen in Fig. (5.6). Effectively, three adjacent injection patterns are performed on the SA specimen. This scheme was explored as an adaptation to overcome potential difficulties detecting dam-

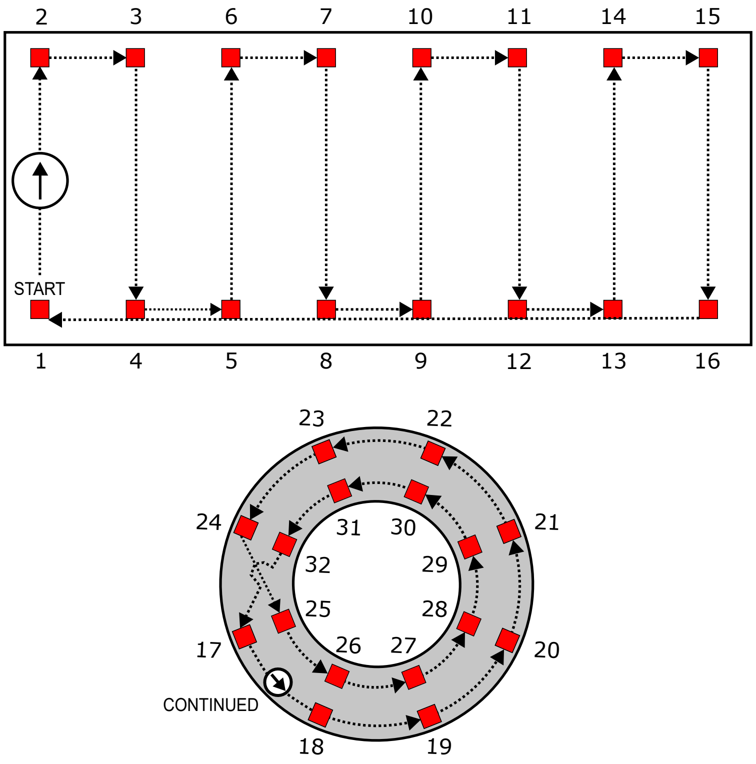

Figure 5.2. Zigzag injection scheme on a 2D projection of the SA specimen.

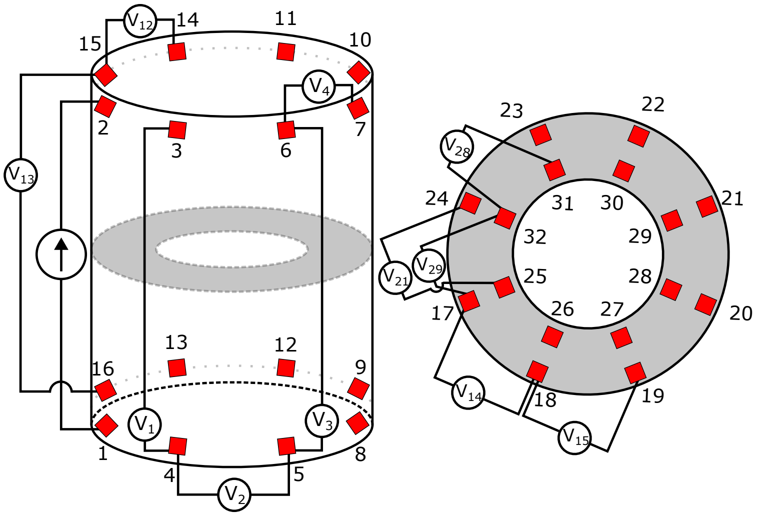

Figure 5.3. Zigzag: First injection and inter-electrode voltage numbering.

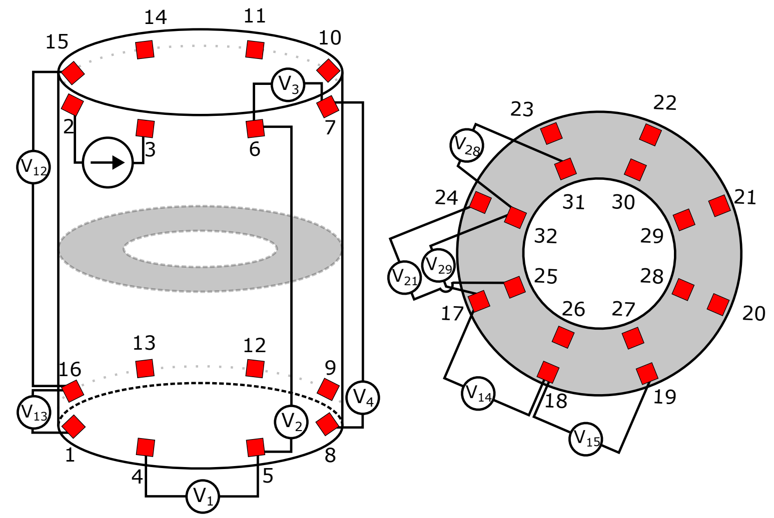

Figure 5.4. Zigzag: Second injection and inter-electrode voltage numbering.

age in complex geometries with multiple surfaces. It was seen in reference [49] that damage far away from electrodes has an observable lower sensitivity for similar damages. In this approach, only the most pertinent electrode data subsets could be used to reduce the computation cost of EIT. The higher electrode density on the annulus likely would not benefit from this modified approach and thus the two concentric rows of electrodes were not treated individually. The process of injection order and inter-electrode voltage differences remains the same. Figures (5.7–5.8) show the first and second current injection pairs with all inter-electrode voltage differences shown. The forward problem is now performed individually for each isolated adjacent injection group, corresponding to each set of experimental data taken. Additionally, $\boldsymbol{J}$ is calculated for each set as well. The proposed modification to the EIT formulation is the concatenation of each $\boldsymbol{V}_m^i$ and $\boldsymbol{J}^i$ used. In other words, Eqn. (5.1 – 5.2) shows how the $\boldsymbol{V}_m$ and $\boldsymbol{J}$ terms are modified.

$$\boldsymbol{V}_m = \begin{bmatrix} \boldsymbol{V}_m^1 \\ \boldsymbol{V}_m^2 \\ \vdots \\ \boldsymbol{V}_m^N \end{bmatrix} \tag{5.1}$$

$$\boldsymbol{J} = \begin{bmatrix} \boldsymbol{J}^1 \\ \boldsymbol{J}^2 \\ \vdots \\ \boldsymbol{J}^N \end{bmatrix} \tag{5.2}$$

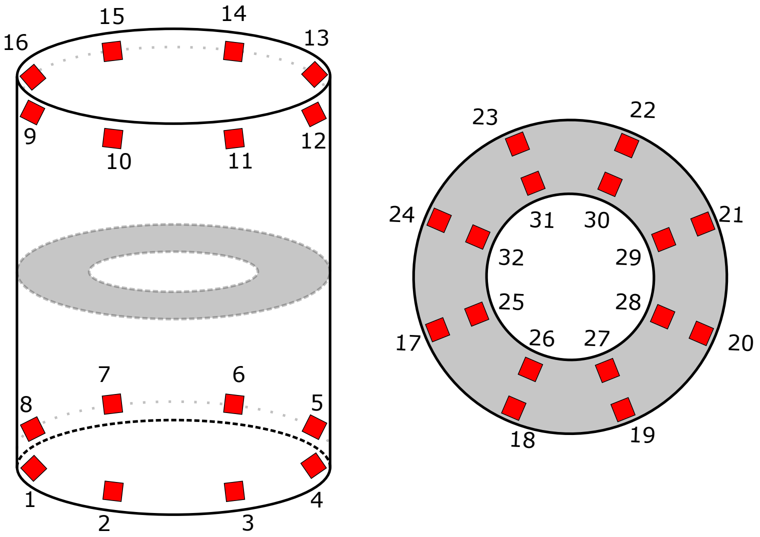

Figure 5.5. Isolated adjacent electrode numbering.

5.4 Impact Test Setup

A CEAST 9340 impact drop tower was used for all impacts done on the SA specimen. The SA specimen was placed on an adjustable base that could be leveled to the impact plane of the test frame. Ideally, the specimens should be securely restrained to maximize the absorbed energy into the test specimen. A carbon-steel v-block was required to elevate the SA specimen for electrode pin clearance and to control the orientation in the test frame due to its cylindrical shape. Steel weights were used to restrict lateral movement and tie-down straps were used to restrict vertical movement. The reasoning behind the additional fixtures was that during testing, the impact energy caused significant recoil movement of the specimen and significantly reduced the desired impact energy. The test setup and specimen loaded into the test frame is shown in Fig. (5.9). The impact tester was used in impact energy control

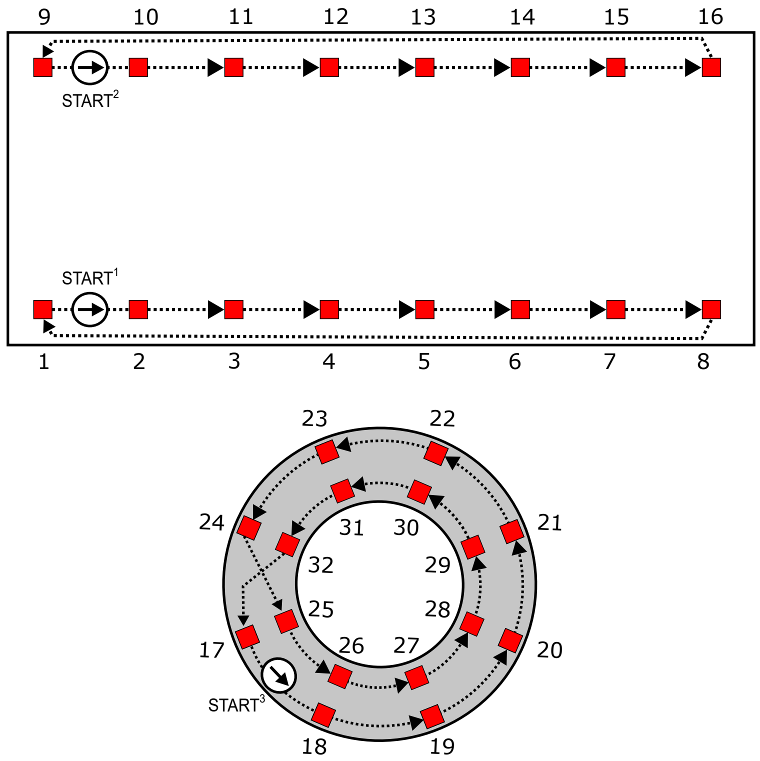

Figure 5.6. Isolated adjacent injection scheme on a 2D projection of the SA specimen.

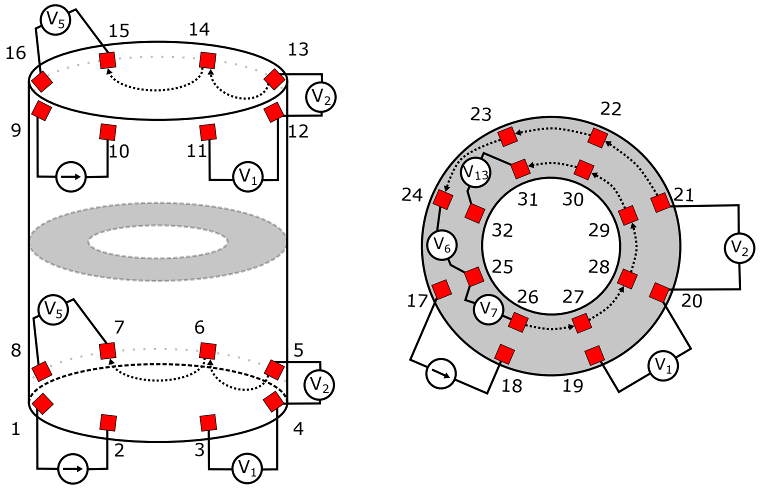

Figure 5.7. Isolated adjacent: First injection and inter-electrode voltage numbering.

and adjusted striker height and velocity accordingly. Verification of the impact energy was done through a photocell installed on the drop tower and the sensor data was analyzed by the control software.

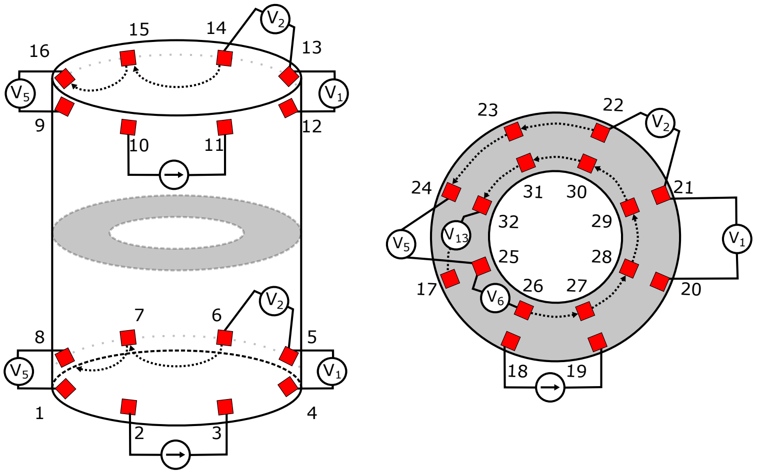

Figure 5.8. Isolated adjacent: Second injection and inter-electrode voltage numbering.

Figure 5.9. a) CEAST impact drop tower, b) SA specimen loaded into test frame with fixturing.

Additionally, an aluminum 6061-T6 insert was inserted into one side of the SA inner volume during impact testing. The reason for the metal insert was for there to be a solid mass behind the thin CFRP laminate thickness. The goal of the impact tests were not to have the impact striker go through the specimen, instead it was to produce BVID. These inserts did provide adequate reinforcement to prevent full fracture of the SA specimens. Visual inspection of the inserts showed that there were indentations from the impacts performed. The inserts were machined from round stock on a Haas ST-20 lathe and turned to the correct dimension to fit snugly within the SA specimen. This machining setup and final result are seen in Fig. (5.10). Each of the two SA specimens required their own metal insert to account for slight dimensional deviations between the laminates.

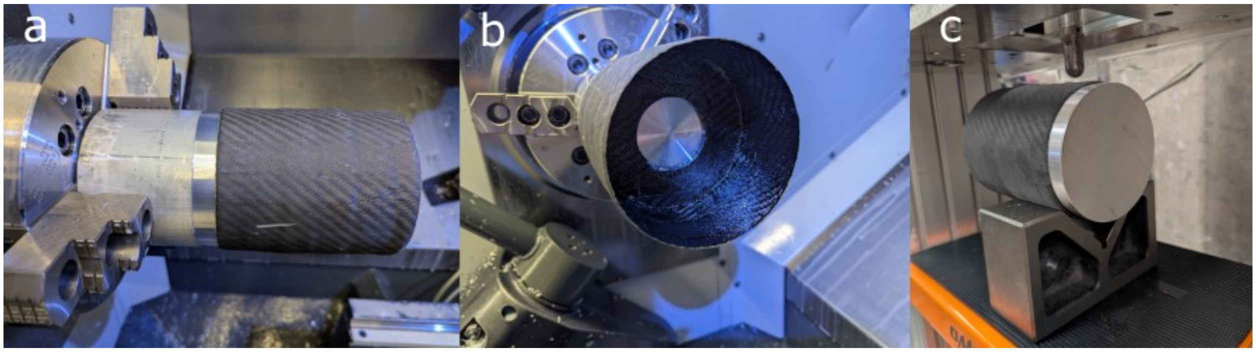

Figure 5.10. a) Fit check of Al6060-T6 insert with SA specimen, b) same fit check from another view, and c) the insert and SA specimen inside the impact drop tower.

5.5 EIT Measurement Setup

A constant 500 (mA) DC current was injected into each electrode pair using a BK Precision 9131B power supply. Voltages from all electrodes were connected via jumper wires and routed through National Instruments (NI) SCB-68A input/output boxes. The signals were captured using NI PXIe-6368 data acquisition system (DAQ) cards. A labVIEW program collected voltage data for 1 second at 200 Hz. The first 100 data points were culled as they contain data where the power supply is adjusting the load of the specimen. Then the remaining data points were averaged. The injection and ground leads were attached to the electrode pins using hook-style leads. The instrumentation setup is shown in Fig. (5.11). A range of currents were explored before settling on 500 (mA). The relatively high conductivity of the CFRP laminate resulted in low signal-to-noise ratio measurements, which makes it more difficult for EIT to correctly reconstruct damage. However, due to the power square law between power and current, $P = I^2$, the current was limited to avoid thermal heating of the injected electrode, causing measured voltages to increase. Since EIT is predicated on difference imaging, it was essential to ensure measurement stability between both states.

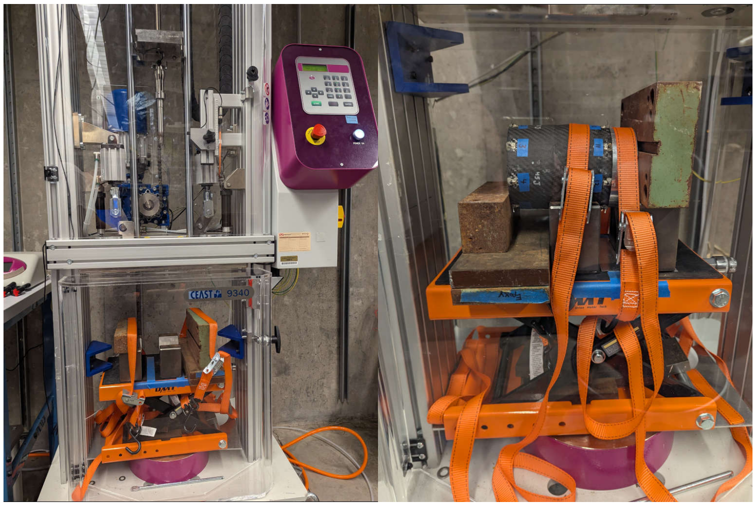

Figure 5.11. Measurement setup of the SA: side view (left) and top view (right).

5.6 Material Conductivity

The EIT formulation relies on an initial conductivity estimate for the piezoresistive material. It is possible to calibrate an initial estimate based on the baseline experimental data. However, it is also advisable to characterize the material through performing conductivity measurements. The following section describes the process and results of conductivity measurements conducted on the material. The selected conductivity for use in the EIT formulation is then presented.

5.6.1 Conductivity Measurements

A DC current of 500 (mA) was injected into each test specimen using a BK Precision 9131B power supply. Voltage was then measured using a Keysight U1241C digital multi-meter (DMM). Four-point wire measurements were used to eliminate lead wire resistances during conductivity measurements due to the low resistance of the test specimens. In Fig. (5.12), hook style leads provided the current injection and the tip probes from the

DMM measured the voltage. Resistance was calculated using Ohm's law $V = IR$, followed by resistivity using the specimen's measured dimensions. Conductivity was calculated as the inverse of resistivity. The average and standard deviation conductivity of five measurements for each type of specimen are shown in Table (5.1). Multiple readings were performed for each measurement to ensure each sample tested was consistent.

An interesting result was that the material's conductivity was not transversely isotropic. A common assumption with bi-directional carbon fiber weaves is that the two planar conductivities are the same since the volumetric average number of fibers aligned with each direction are the same. Fibers in isolation exhibit orthotropic conductivity and it was also reported in reference [30], that fiber orientation matters for conductivity. The differences in measured planar conductivities may have a few explanations. First, there could be a general misalignment of the fibers with the way the test specimens were cut. Square tools were used to cut the prepreg and laminate, aiding ply and specimen alignment during manufacturing. Visual inspection also did not indicate a significant fiber angle misalignment, but this was a qualitative assessment only. Second, it could be that this specific bi-directional CFRP prepreg exhibits orthotropic behavior. The prepreg was cut in a methodical manner to ensure the layup angles were followed, but each ply was not necessarily laid in the same orientation from which it was cut from the prepreg roll. Therefore, it is not possible to definitively conclude orthotropic properties is the norm for this material. Finally, it was observed that the fibers from the prepreg were not well aligned from the supplier. Figure (5.13) shows that the weave had numerous fiber separation gaps with curved fibers and a general lack of uniform fiber spacing. It is possible that enough fibers were misaligned in the sample specimens to affect the anisotropic behavior. The values measured for each specimen type were consistent, as seen by the reported standard deviations for the planar values. A noted exception to this statement is the through-thickness values had a larger deviation among measured specimens. The fiber misalignment could have exacerbated measurements in the through-thickness direction given the wide range of values measured. More research into CFRP prepreg laminates will need to be done to have a better understanding of the electrical conductivity.

An average conductivity value along the x_1 direction was calculated to be $2,268$ ($\mathrm{S\,m^{-1}}$), with a standard deviation of $\pm$ 125 ($\mathrm{S\,m^{-1}}$). An average conductivity value along the x_2 direction was calculated to be $1,323$ ($\mathrm{S\,m^{-1}}$), with a standard deviation of $\pm$ 215 ($\mathrm{S\,m^{-1}}$). An average thru-thickness conductivity value was calculated to be 0.35 ($\mathrm{S\,m^{-1}}$), with a standard deviation of $\pm$ 0.169 ($\mathrm{S\,m^{-1}}$). The results are presented in SI units to follow the common convention of presenting conductivity in EIT literature.

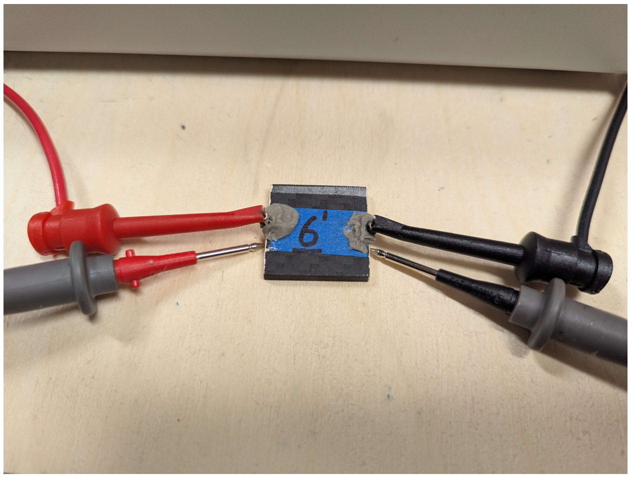

Figure 5.12. Conductivity specimen test setup.

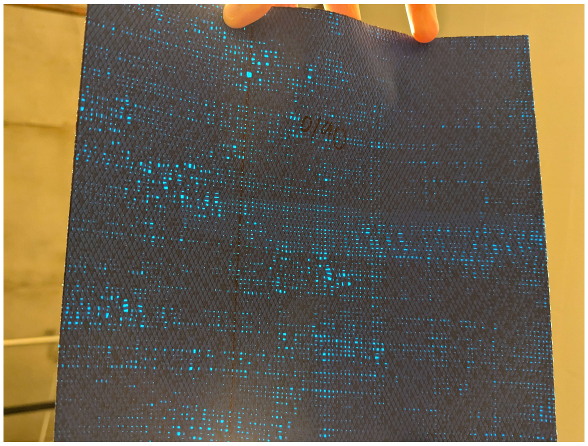

Figure 5.13. Carbon fiber prepreg held to the light to show general fiber misalignment and gaps.

Table 5.1. Conductivity measurements in all three principle axes with standard deviation.

Direction	Average
σ_{x_1}	2268 ± 125 ($\mathrm{S\,m^{-1}}$)
σ_{x_2}	1323 ± 215 ($\mathrm{S\,m^{-1}}$)
σ_{x_3}	0.35 ± 0.169 ($\mathrm{S\,m^{-1}}$)

5.6.2 Conductivity Selection

Based on the conductivity measurements, the material conductivity tensor is shown in Eqs. (5.3 – 5.4). The initial assumption that the prepreg CFRP exhibits transversely isotropic conductivity was not supported by data and instead measured orthotropic properties. Additionally, there was uncertainty which direction would be appropriate for each respective conductivity scalar. Therefore, EIT routines were ran, alternating between the two planar conductivity values. Both produced qualitatively similar reconstruction images so only one tensorial form is presented below. Finally, separate conductivity tensors were used for the shell and annulus respectively. The appropriate tensor was selected based if the radial distance of an elemental centroid was past the O.D. of the annulus as described in Section (3.7).

$$\boldsymbol{\sigma}_{ij}^{\text{shell}} = \begin{bmatrix} 0.35 & 0 & 0 \\ 0 & 1323 & 0 \\ 0 & 0 & 2366 \end{bmatrix} (\mathrm{S\,m^{-1}}) \tag{5.3}$$

$$\boldsymbol{\sigma}_{ij}^{\text{annulus}} = \begin{bmatrix} 2366 & 0 & 0 \\ 0 & 1323 & 0 \\ 0 & 0 & 0.35 \end{bmatrix} (\mathrm{S\,m^{-1}}) \tag{5.4}$$

6. EXPERIMENTAL RESULTS

This chapter contains the results of experimental damage detection of a geometrically-complex, non-planar CFRP laminate using EIT. First, notch damage detection will be described. Second, impact damage detection will be presented. The reconstructions, except the PDIPM result, are normalized by the initial estimate of κ and presented as a percent. The PDIPM result is presented as the change in conductivity ($\mathrm{S\,m^{-1}}$).

6.1 Notch Damage Reconstruction

Notch damage is easier to detect in EIT reconstructions because the severance of carbon fibers significantly increases resistivity and an excellent first test to validate the EIT formulation. A notch was cut into the annulus between electrodes 30 and 31 using a Dremel rotary cutting tool, as seen in Fig. (6.1). The size of this notch was 0.15 (in.) wide and 0.36 (in.) in length. Figure (6.2) shows the notch damage in the SA annulus with the length of the notch measured. The orthotropic conductivity tensor formulation was used with the zigzag injection scheme. Finally, the EIT damage reconstruction image can be seen in Fig. (6.3).

From inspection of the EIT reconstruction, the formulation captured the damage well. The location of the damage was correctly found and the predicted conductivity loss was shaped appropriately. The notch did not extend past the inner electrode ring, and similarly the predicted loss also does not extend past this reference line. Additionally, there was an absence of noise or artifacts everywhere else on the domain, indicating a stability in measurements taken. The conductivity loss is presented as a percentage normalized by the value of κ used to constrain the minimization. This lack of noise was also likely due to the aforementioned relative ease of finding notch damage.

6.2 Impact Damage: 18 (J)

The next damage to be detected was a 18 (J) impact located near electrodes one and four. Detecting impact damage is more of a challenge to detect because generally the loss of conductivity is smaller than from notch damage. Fewer fibers break and prepregs have

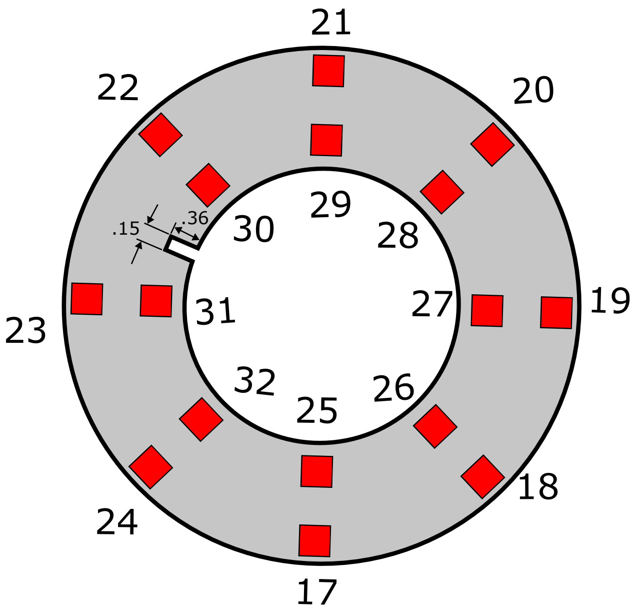

Figure 6.1. Location and sizing of notch damage in annulus, dimensions in (in.) (Not to scale).

Figure 6.2. Annulus after cutting of the notch with the length verification.

less excess resin susceptible to matrix cracking, leading to smaller differences between the baseline and damaged electrode voltages. The impact left a visible indentation approximately 0.21 × 0.27 (in.) in size and located 1.625 (in.) from the bottom plane of the specimen. The impact measurements can be seen in Fig. (6.4). On the surface, a clear impression from the impact striker could be seen. It was not clear if crack propagated through the thickness of

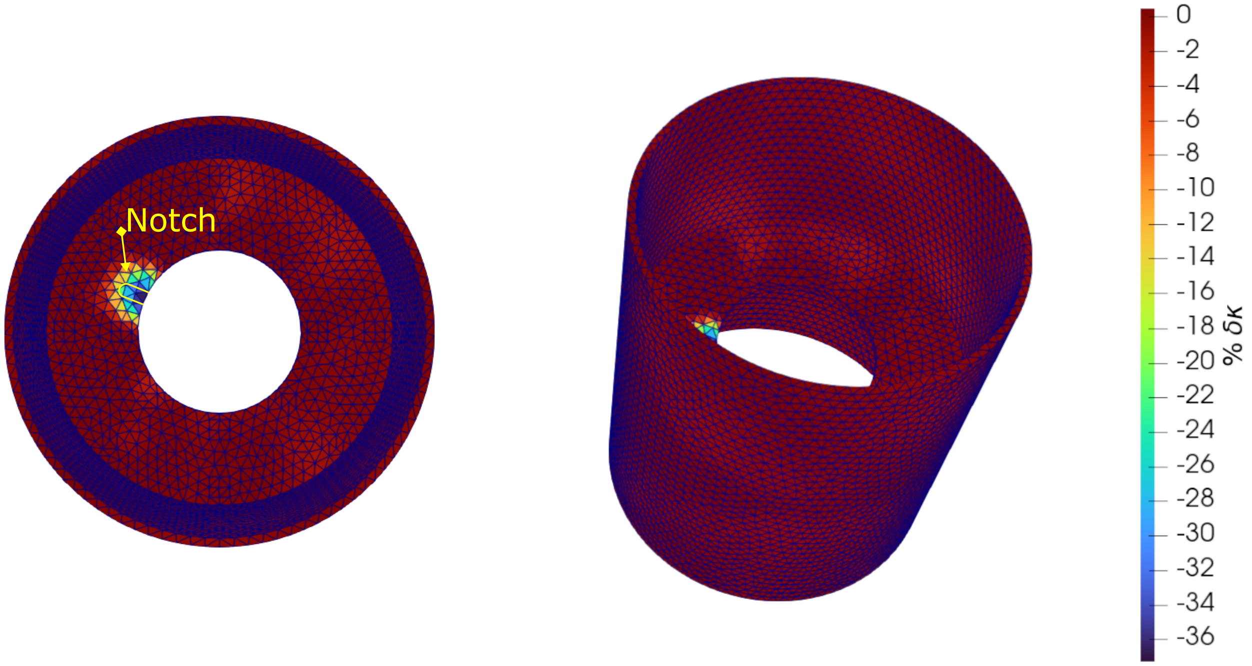

Figure 6.3. EIT reconstruction: annulus notch damage, orthotropic tensor, zigzag scheme.

the laminate. Once again, the orthotropic conductivity tensor formulation was used with the zigzag injection scheme. Finally, the EIT damage reconstruction image can be seen in Fig. (6.5).

The resulting reconstruction was not as clearly defined as the notch damage reconstruction. First, the location of the largest predicted conductivity loss was in the general location, but not shaped well. More specifically, the damage was placed between the correct electrodes in the lower left of the image, indicated by the yellow circle, but was leaned towards the bottom edge of the domain, as indicated by Fig. (6.4). There is also the addition of experimental noise or artifacts throughout the image in the best recoverable reconstruction. While it is tempting to say the damage was identified based on *a priori* knowledge about the damage, the degree of noise prevents conclusive identification of the damage to the author. The largest predicted loss was in the range of 2.8% and was significantly smaller than the 36% loss from the notch reconstruction. Again, it is stated the loss is presented as a percent change normalized by κ. This lower predicted conductivity loss could have exacerbated the degree of noise from experimental data.

Several observations were taken from the 18 (J) impact test. The first was perhaps the impact energy was not high enough to produce enough fracture damage to the CFRP laminate. The surface indentation observed appeared very localized, but the extent of damage was not characterized by other NDE methods. Second, the noise seen in the reconstructed image could be an indication of electrode damage. Certainly the electrodes responded appropriately post-impact to the current injections and there was no visible damage seen. The cause of potential electrode damage could have been from the impact itself. A limitation of EIT is the sensitivity to outlier data, coupled with the ℓ_2-norm favoring smoothly varying solutions. Increases to the contact impedance could have led the least-squares minimization to produce false-positive damage detection in areas not physically meaningful. Finally, review of the injection scheme highlighted a potential damage sensitivity issue. The damage was conducted in a location that was not in a direct *path* for a current injection or inter-electrode difference. This configuration could have led to the current-voltage relationship being minimally affected by the damage. It was possible that the coupled factors of the impact energy, impact location, injection scheme, and fracture toughness of the prepreg CFRP resulted in low damage sensitivity.

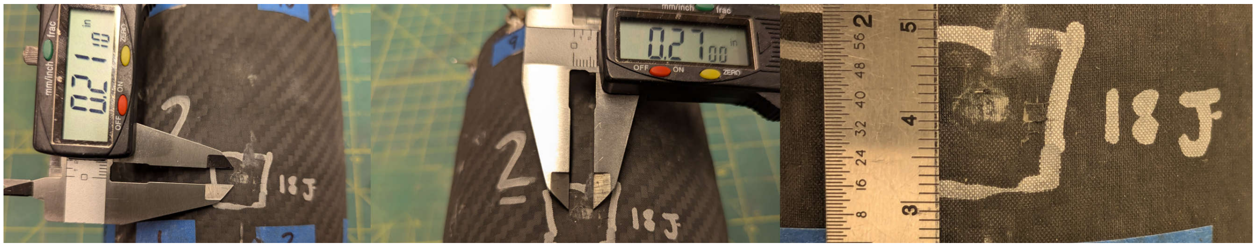

Figure 6.4. Location and sizing of 18 (J) impact damage in shell, dimensions in (in.).

6.3 Impact Damage: 46 (J)

In light of the 18 (J) impact results, an additional impact test was conducted on the shell. In the second impact test, the impact energy was significantly increased and the

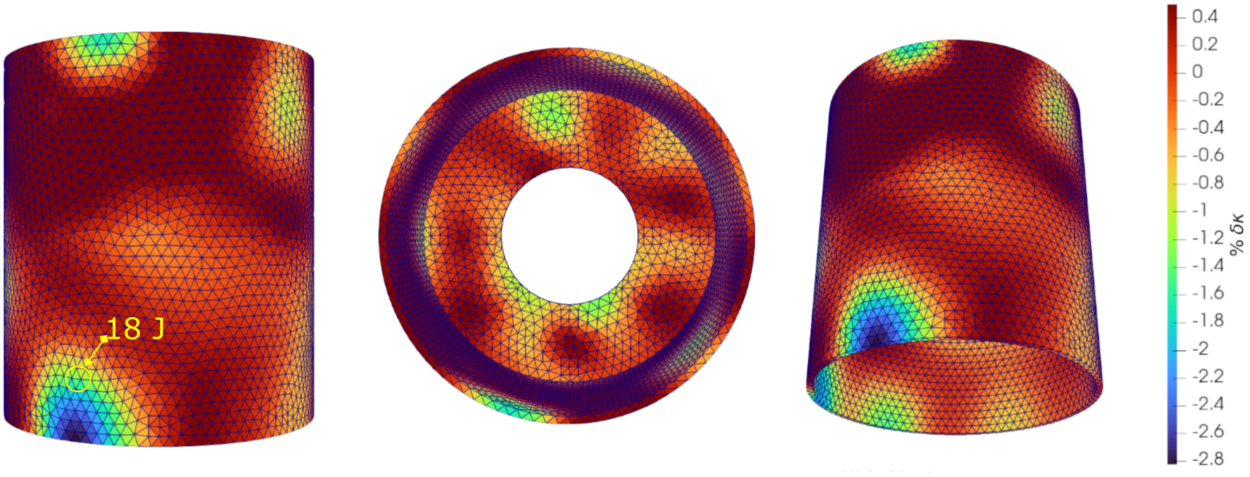

Figure 6.5. EIT reconstruction: shell 18 (J) impact damage, orthotropic tensor, zigzag scheme.

isolated injection scheme was utilized. Increasing the impact energy should increase the probability of detection through a measurable current-voltage relationship at the electrodes. The location of impact was selected to be in close relative proximity of current injection and inter-electrode differences. The orthotropic conductivity formulation was used with the isolated adjacent injection scheme. Additionally, measurements were only conducted using the 16 electrodes located on the shell with the 16 electrodes in the annulus excluded.

An impact energy of 46 (J) was impacted located near electrodes 9 and 10. Note this was using the electrode numbering of the isolated adjacent scheme. Once again, the impact left a visible indentation measuring 0.25×0.29 (in.) in size and located 4.75 (in.) from the bottom plane of the specimen. The impact measurements can be seen in Fig. (6.6). The higher energy resulted in a slightly larger damage size compared to the 18 (J) impact, but of comparable size despite the energy being over 2.5 times higher in magnitude. The damage reconstruction can be seen in Fig. (6.7) with the damage located in the upper left of the image highlighted by the yellow circle.

The results in the EIT image show marked improvement from the 18 (J) reconstruction. The location of the impact was located correctly between electrodes 9 and 10. With the damage being closer to the edge of the specimen, there was a max predicted loss centered at the edge. The noise in the image was significantly less with the exception of some predicted loss in regions without physical damage. However, the conductivity loss was much larger with respect to noise, supporting a more conclusive identification of the damage. Additionally, the predicted percent loss of conductivity 65% with the noisy regions having losses in the 35% range.

The results from the second impact test provided additional insights from observations made after the first impact. The higher impact energy was reflected in a higher magnitude of predicted loss. The presence of noise now concentrated near the edges supports the theory of minor electrode damage due to impact testing. The same skewing of the damage centering was still present like in the 18 (J) impact. Finally, the implementation of the isolated adjacent injection scheme for EIT appeared to result in an acceptable image.

It needs to be noted that electrode six was sheared off after the 46 (J) impact. This was noticed before the damaged data set was collected, but a new baseline data set was not remeasured. The electrode surface on the shell was sanded to remove residue. Care was taken to leave a outline of the original electrode square to help align painting the new electrode over the old electrode location. It was unclear how much this replacement affected the measurements and ensuing EIT reconstruction.

Figure 6.6. Location and sizing of 46 (J) impact damage in shell, dimensions in (in.).

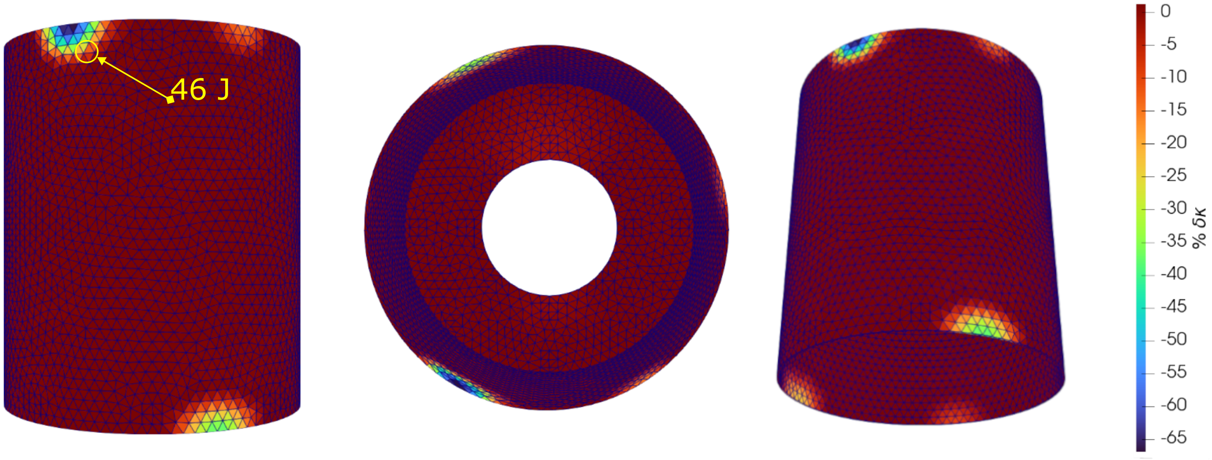

Figure 6.7. EIT reconstruction: shell 46 (J) impact damage, orthotropic tensor, isolated adjacent scheme.

6.3.1 PDIPM Error Minimization with Homogeneous Best-Fit

Although the previous result was an improvement over the 18 (J) case, additional work was done to see if the EIT reconstruction could be improved. To that end, the EIT inverse problem was instead solved by minimizing the ℓ_1-norm of the error via the PDIPM algorithm. The ℓ_1-norm improves EIT reconstructions through robustness to outlier data and the previous result indicated noise from potential damage to electrodes. The other change was instead of using the conductivity measurements to define the baseline conductivity tensor estimate, a homogeneous best fit was done using the baseline experimental data. In other words, the predicted voltages from the forward problem are compared the the experimental voltages of the SA specimen in the baseline state. A range of conductivity values are supplied to the forward problem and the conductivity that resulted in the smallest residual between the model and experimental data was selected. The best homogeneous fit was with a conductivity value of 6,000 ($\mathrm{S\,m^{-1}}$) and the resulting plot between the model and experimental data is shown in Fig. (6.8). From this plot, the experimental data consistently had values larger than the model, further suggesting the presence of electrode damage.

The same 46 (J) impact damage data was used with the modified EIT formulation. As seen in Fig. (6.9), the reconstructed image was improved from the previous ℓ_2-norm approach. Namely, the artifacts not representative of physical damage have been eliminated from the image, leaving only the impact damage with a predicted conductivity loss. The gradient of predicted loss also matches the reality of the impact location better. Additionally, the maximum predicted loss was approximately -177 ($\mathrm{S\,m^{-1}}$). It is noted that the value reported for the ℓ_1-norm minimization is not normalized by κ and is instead the change in conductivity. Figure (6.10) shows the convergence of the PDIPM, with the relative residual and error converging after three iterations. The damage size was larger than the previous EIT formulation. The improved image demonstrated the difference the ℓ_1-norm had on robustness to noise and provided further indication that electrode damage skewed results from the ℓ_2-norm minimization.

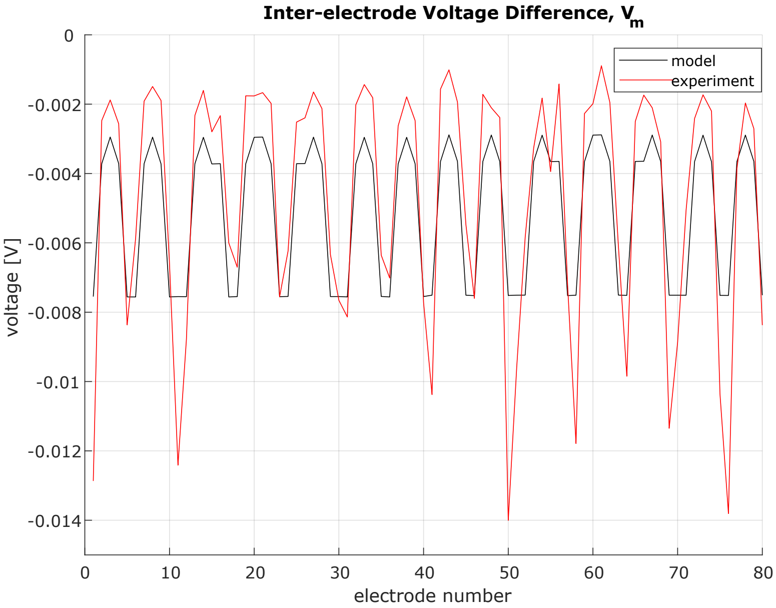

Figure 6.8. Comparison between best-fit conductivity model predicted and experimental baseline inter-electrode voltage differences.

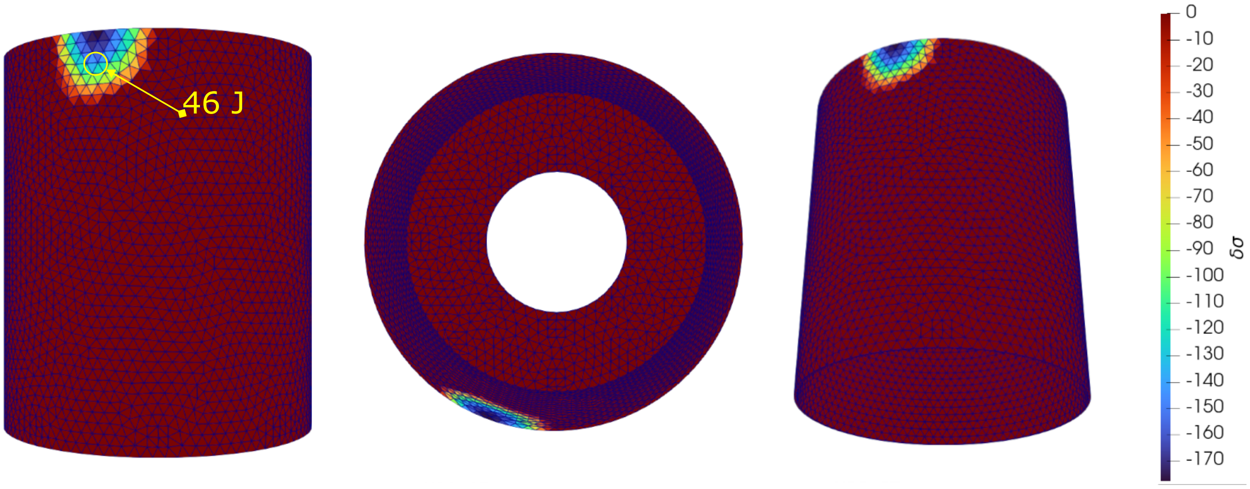

Figure 6.9. EIT reconstruction: shell 46 (J) impact damage, homogeneous best fit conductivity, PDIPM error minimization, isolated adjacent scheme.

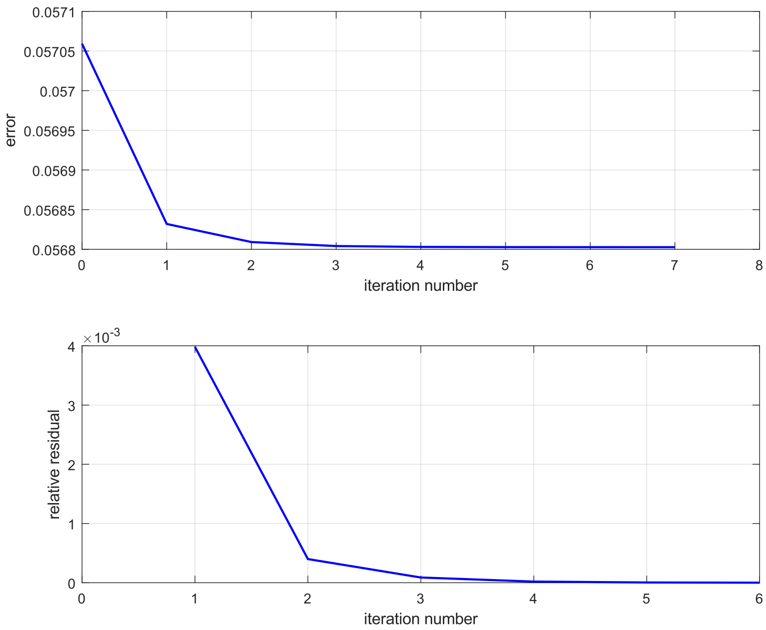

Figure 6.10. Convergence plot of the PDIPM algorithm showing error and relative residual per iteration.

7. SUMMARY, CONCLUSIONS, AND FUTURE WORK

This chapter includes a brief summary of the work presented in this thesis. Several conclusions are stated from the results of the EIT mathematical formulation and experiments. Finally, a brief discussion is presented on recommended future work.

7.1 Summary

The motivation of this research was to advance the state-of-the-art for damage detection of self-sensing CFRP laminates that are geometrically complex using EIT for potential future embedded sensing systems. CFRP laminates are commonly used in the design of high performance aerospace structures. While NDE methods exist to detection damage in a laboratory or maintenance environment, there is currently no practical method of detecting damage of CFRPs once in service. Additionally, EIT research must move beyond applications on flat plates towards laminates more representative of real world structures. Carbon fiber is also a piezoresistive material worth researching for embedded sensing systems because no modifications are required to the laminate that would sacrifice structural performance.

A CFRP laminate was manufactured as a cylindrical shell structure with an internal annulus for use in EIT damage detection experiments. The geometry was designed to be a generic structural composite laminate. Although there was no specific application of this laminate that guided the shape, the laminate should have reasonable strength to general loading conditions. The material's conductivity was calculated based on four-point wire measurements.

Several damage modes were inflicted onto the specimen to determine the efficacy of self-sensing damage detection to each damage. First, a small rectangular notch was cut out from the annulus. The developed anisotropic EIT formulation successfully detected this damage clearly without the presence of outlier noise. Next, two impact events were performed on the test specimen to mimic BVID. The first impact at 18 (J) was not conclusively found like the notch. The predicted conductivity loss was generally in the correct location, but noise permeated the reconstruction image that did not match physical damage. It is hypothesized the inability to clearly find this damage was largely a consequence of the injection-measurement scheme. That is, the damage just so happened to be placed in a region through which little current flowed. The next impact was done at 46 (J) and using a different injection scheme to improve damage detection. The damage was found with significantly less noise, meaning the detection capability improved. The presence of noise in the regions close to the electrodes support the idea of progressive electrode data.

Finally, a ℓ_1-norm error minimization using a PDIPM algorithm was used with a experimentally calibrated homogeneous best-fit conductivity to generate another EIT reconstruction of the same 46 (J) impact. Improvements in the ℓ_1-norm result shows the significance of outlier data with the ℓ_2-norm formulation. The two results generally agree, but the ℓ_1-norm produced the superior and noiseless damage reconstruction.

7.2 Conclusion

In conclusion, this work presents the capabilities and challenges of performing EIT on a CFRP prepreg laminate with geometric complexities. EIT is capable of detecting notch damage very effectively, but impact damage is harder to detect due lower signal-to-noise ratios. Noisy data exacerbates this difficulty and gives credence to favor the ℓ_1-norm instead of the ℓ_2-norm for EIT applications . Because little research has been done on EIT with CFRP prepreg laminates with this complexity, the work presented herein is important towards understanding effective strategies for damage detection and considerations to avoid and minimize experimental noise. Additionally, a different injection scheme was required to improve detection sensitivity. This work demonstrates that EIT is capable of detecting damage several damage types within CFRP prepregs to advance the state-of-the-art of self-sensing structures.

7.3 Future Work

More research is needed in understanding the specific behaviors of prepreg CFRPs for self-sensing applications. A lot of work had been conducted using dry fabric for laminates, whereas this work uses prepregs. The added fracture toughness of prepregs likely reduced the observed resistance changes within test specimens and negatively affected the clarity of reconstruction images. A sensitivity experiment comparing the difference in damage detection of the same weave patterns, dry versus prepreg, would help determine impact energy detectability limitations. Additionally, characterizing the anisotropic conductivity of multiple commercially available prepreg CFRP materials would help set expectations of values for EIT research. Comparable work by Sannamani et. al [48] presented conductivity values significantly different than those in this work. With more data sets that can be referenced, experimental results can be either correlated or highlight emergent observations.

A pernicious challenge for EIT as a successful damage detection modality is robust electrodes. The damage detection capabilities in this work certainly were affected. Noise was persistent in the data, likely from impact loading. However, visually the electrodes appeared unharmed. An electrode configuration with a low profile or low mass could help prevent degradation.

REFERENCES

[1] K. D. Challenger. “The damage tolerance of carbon fiber reinforced compositesA workshop summary”. In: *Composite Structures* 6.4 (Jan. 1, 1986), pp. 295–318. ISSN: 0263-8223. DOI: 10.1016/0263-8223(86)90025-5.

[2] Roger Groves. “3.12 Inspection and Monitoring of Composite Aircraft Structures”. In: *Reference Module in Materials Science and Materials Engineering*. Vol. 3. Reference Module in Materials Science and Materials Engineering II. Elservier, 2018, pp. 300–311. ISBN: 978-0-12-803581-8. DOI: 10.1016/B978-0-12-803581-8.10340-6.

[3] Elaheh Sabziyan Varnousfaderani and Syed A. M. Shihab. “Bird strikes in aviation: A systematic review for informing future directions”. In: *Aerospace Science and Technology* 163 (Aug. 1, 2025), p. 110303. ISSN: 1270-9638. DOI: 10.1016/j.ast.2025.110303.

[4] Ranjeetkumar Gupta et al. “A Review of Sensing Technologies for Non-Destructive Evaluation of Structural Composite Materials”. In: *Journal of Composites Science* 5.12 (Dec. 2021). Number: 12 Publisher: Multidisciplinary Digital Publishing Institute, p. 319. ISSN: 2504-477X. DOI: 10.3390/jcs5120319.

[5] Ramesh S. Sharma and M. N. Vijayakumar. “Recent Developments in Damage Detection of CFRP Composites Using Non-Destructive Techniques A Review”. In: *Journal of Engineering Research and Reports* 25.4 (June 22, 2023), pp. 51–65. ISSN: 2582-2926. DOI: 10.9734/jerr/2023/v25i4902.

[6] M. Q. Feng, G. Roqueta, and L. Jofre. “22 - Non-destructive evaluation (NDE) of composites: microwave techniques”. In: *Non-Destructive Evaluation (NDE) of Polymer Matrix Composites*. Ed. by Vistasp M. Karbhari. Woodhead Publishing Series in Composites Science and Engineering. Woodhead Publishing, Jan. 1, 2013, pp. 574–616. ISBN: 978-0-85709-344-8. DOI: 10.1533/9780857093554.4.574.

[7] Sahar Hassani, Mohsen Mousavi, and Amir H. Gandomi. “Structural Health Monitoring in Composite Structures: A Comprehensive Review”. In: *Sensors* 22.1 (Jan. 2022). Publisher: Multidisciplinary Digital Publishing Institute, p. 153. ISSN: 1424-8220. DOI: 10.3390/s22010153.

[8] Opukuro David-West et al. “A Review of Structural Health Monitoring Techniques as Applied to Composite Structures”. In: *Structural Durability & Health Monitoring* 11.2 (Oct. 1, 2017). Num Pages: 57, pp. 91–147. DOI: 10.3970/sdhm.2017.011.091.

[9] Siti Musliha Aishah Musa et al. “Embedded and Surface-Mounted Fiber Bragg Grating as a Multiparameter Sensor in Fiber-Reinforced Polymer Composite Materials: A Review”. In: *IEEE Access* 11 (2023), pp. 86611–86644. ISSN: 2169-3536. DOI: 10.1109/ACCESS.2023.3304679.

[10] Riwu Yao, Jianfeng Shi, and Jinyang Zheng. “Curing quality monitoring and loading detection of composite structures with embedded capacitive sensor array”. In: *Materials & Design* 213 (Jan. 1, 2022), p. 110321. ISSN: 0264-1275. DOI: 10.1016/j.matdes.2021.110321.

[11] Arnaud Huijer et al. “Feasibility evaluation for development of composite propellers with embedded piezoelectric sensors”. In: *Marine Structures* 84 (July 1, 2022), p. 103231. ISSN: 0951-8339. DOI: 10.1016/j.marstruc.2022.103231.

[12] Maryam Kahali Moghaddam et al. “Embedding Piezoresistive Pressure Sensors to Obtain Online Pressure Profiles Inside Fiber Composite Laminates”. In: *Sensors* 15.4 (Apr. 2015). Publisher: Multidisciplinary Digital Publishing Institute, pp. 7499–7511. ISSN: 1424-8220. DOI: 10.3390/s150407499.

[13] R. Janeliukstis and D. Mironovs. “Smart Composite Structures with Embedded Sensors for Load and Damage Monitoring A Review”. In: *Mechanics of Composite Materials* 57.2 (May 1, 2021), pp. 131–152. ISSN: 1573-8922. DOI: 10.1007/s11029-021-09941-6.

[14] Sihai Wen and D. D. L. Chung. “Electrical-resistance-based damage self-sensing in carbon fiber reinforced cement”. In: *Carbon* 45.4 (Apr. 1, 2007), pp. 710–716. ISSN: 0008-6223. DOI: 10.1016/j.carbon.2006.11.029.

[15] Wengui Li et al. “A comprehensive review on self-sensing graphene/cementitious composites: A pathway toward next-generation smart concrete”. In: *Construction and Building Materials* 331 (May 9, 2022), p. 127284. ISSN: 0950-0618. DOI: 10.1016/j.conbuildmat.2022.127284.

[16] Bryan R. Loyola, Valeria La Saponara, and Kenneth J. Loh. “Characterizing the self-sensing performance of carbon nanotube-enhanced fiber-reinforced polymers”. In: *Nondestructive Characterization for Composite Materials, Aerospace Engineering, Civil Infrastructure, and Homeland Security 2010*. Nondestructive Characterization for Composite Materials, Aerospace Engineering, Civil Infrastructure, and Homeland Security 2010. Vol. 7649. SPIE, Mar. 25, 2010, pp. 109–120. DOI: 10.1117/12.848712.

[17] Long Wang and Kenneth J Loh. “Wearable carbon nanotube-based fabric sensors for monitoring human physiological performance”. In: *Smart Materials and Structures* 26.5 (Apr. 2017). Publisher: IOP Publishing, p. 055018. ISSN: 0964-1726. DOI: 10.1088/1361-665X/aa6849.

[18] Francesca Nanni et al. “Effect of carbon black nanoparticle intrinsic properties on the self-monitoring performance of glass fibre reinforced composite rods”. In: *Composites Science and Technology* 71.1 (Jan. 1, 2011), pp. 1–8. ISSN: 0266-3538. DOI: 10.1016/j.compscitech.2010.08.015.

[19] Tyler N Tallman et al. “Damage detection via electrical impedance tomography in glass fiber/epoxy laminates with carbon black filler”. In: *Structural Health Monitoring* 14.1 (Jan. 1, 2015). Publisher: SAGE Publications, pp. 100–109. ISSN: 1475-9217. DOI: 10.1177/1475921714554142.

[20] André O. Monteiro, Paulo B. Cachim, and Pedro M. F. J. Costa. “Self-sensing piezoresistive cement composite loaded with carbon black particles”. In: *Cement and Concrete Composites* 81 (Aug. 1, 2017), pp. 59–65. ISSN: 0958-9465. DOI: 10.1016/j.cemconcomp.2017.04.009.

[21] Miguel Ramirez and D. D. L. Chung. "Electromechanical, self-sensing and viscoelastic behavior of carbon fiber tows". In: *Carbon* 110 (Dec. 1, 2016), pp. 8–16. ISSN: 0008-6223. DOI: 10.1016/j.carbon.2016.08.095.

[22] Patrick Scholle and Michael Sinapius. "A Review on the Usage of Continuous Carbon Fibers for Piezoresistive Self Strain Sensing Fiber Reinforced Plastics". In: *Journal of Composites Science* 5.4 (Apr. 2021). Publisher: Multidisciplinary Digital Publishing Institute, p. 96. ISSN: 2504-477X. DOI: 10.3390/jcs5040096.

[23] Shu-Yang Wang et al. "A Review on Resistance-Based Self-Sensing of Carbon Fiber-Reinforced Polymer Subjected to Loads". In: *Advanced Engineering Materials* 27.13 (2025). _eprint: https://advanced.onlinelibrary.wiley.com/doi/pdf/10.1002/adem.202500244, p. 2500244. ISSN: 1527-2648. DOI: 10.1002/adem.202500244.

[24] Tomo Takeda et al. "Modeling and characterization of the electrical conductivity of carbon nanotube-based polymer composites". In: *Polymer* 52.17 (Aug. 3, 2011), pp. 3852–3856. ISSN: 0032-3861. DOI: 10.1016/j.polymer.2011.06.046.

[25] Ali Esmaeili et al. "Piezoresistive characterization of epoxy based nanocomposites loaded with SWCNTs-DWCNTs in tensile and fracture tests". In: *Polymer Composites* 41.7 (2020). _eprint: https://4spepublications.onlinelibrary.wiley.com/doi/pdf/10.1002/pc.25558, pp. 2598–2609. ISSN: 1548-0569. DOI: 10.1002/pc.25558.

[26] J. J. Ku-Herrera and F. Avilés. "Cyclic tension and compression piezoresistivity of carbon nanotube/vinyl ester composites in the elastic and plastic regimes". In: *Carbon* 50.7 (June 1, 2012), pp. 2592–2598. ISSN: 0008-6223. DOI: 10.1016/j.carbon.2012.02.018.

[27] Gustavo Henrique Nalon et al. "Effects of different kinds of carbon black nanoparticles on the piezoresistive and mechanical properties of cement-based composites". In: *Journal of Building Engineering* 32 (Nov. 1, 2020), p. 101724. ISSN: 2352-7102. DOI: 10.1016/j.jobe.2020.101724.

[28] Hyung Doh Roh and Young-Bin Park. "Carbon fiber grid sensor for structural deformation using piezoresistive behavior of carbon fiber". In: *Sensors and Actuators A: Physical* 341 (July 1, 2022), p. 113348. ISSN: 0924-4247. DOI: 10.1016/j.sna.2021.113348.

[29] Yusuke Nishio et al. "Piezoresistive effect of plain-weave CFRP fabric subjected to cyclic loading". In: *Advanced Composite Materials* 26.3 (May 4, 2017). Publisher: Taylor & Francis _eprint: https://doi.org/10.1080/09243046.2016.1239354, pp. 229–243. ISSN: 0924-3046. DOI: 10.1080/09243046.2016.1239354.

[30] N. Athanasopoulos and V. Kostopoulos. "Prediction and experimental validation of the electrical conductivity of dry carbon fiber unidirectional layers". In: *Composites Part B: Engineering* 42.6 (Sept. 1, 2011), pp. 1578–1587. ISSN: 1359-8368. DOI: 10.1016/j.compositesb.2011.04.008.

[31] L. Guadagno et al. "Correlation between electrical conductivity and manufacturing processes of nanofilled carbon fiber reinforced composites". In: *Composites Part B: Engineering* 80 (Oct. 1, 2015), pp. 7–14. ISSN: 1359-8368. DOI: 10.1016/j.compositesb.2015.05.025.

[32] Xiang Xi and D. D. L. Chung. "Colossal electric permittivity discovered in polyacrylonitrile (PAN) based carbon fiber, with comparison of PAN-based and pitch-based carbon fibers". In: *Carbon* 145 (Apr. 1, 2019), pp. 734–739. ISSN: 0008-6223. DOI: 10.1016/j.carbon.2019.01.069.

[33] Xiang Xi and D. D. L. Chung. "Piezoelectric and piezoresistive behavior of unmodified carbon fiber". In: *Carbon* 145 (Apr. 1, 2019), pp. 452–461. ISSN: 0008-6223. DOI: 10.1016/j.carbon.2019.01.044.

[34] Jos\{{\textbackslash}'e\} de Jes\{'u\}s Ku Herrera et al. "Piezoresistive Sensing of Strain and Damage in Carbon/Epoxy Rectangular and I-shaped Cross-section Beams in Flexure". In: *Journal of Multifunctional Composites* 2 (2014), pp. 171–181.

[35] G. M. Koo and T. N. Tallman. "Higher-order resistivity-strain relations for self-sensing nanocomposites subject to general deformations". In: *Composites Part B: Engineering* 190 (June 1, 2020), p. 107907. ISSN: 1359-8368. DOI: 10.1016/j.compositesb.2020.107907.

[36] R. J. Lytle and K. A. Dines. *Impedance camera: a system for determining the spatial variation of electrical conductivity*. UCRL-52413. California Univ., Livermore (USA). Lawrence Livermore Lab., Jan. 30, 1978. DOI: 10.2172/6753686.

[37] Ross P. Henderson and John G. Webster. "An Impedance Camera for Spatially Specific Measurements of the Thorax". In: *IEEE Transactions on Biomedical Engineering* BME-25.3 (May 1978), pp. 250–254. ISSN: 1558-2531. DOI: 10.1109/TBME.1978.326329.

[38] Zifei Xu et al. "Development of a Portable Electrical Impedance Tomography System for Biomedical Applications". In: *IEEE Sensors Journal* 18.19 (Oct. 2018), pp. 8117–8124. ISSN: 1558-1748. DOI: 10.1109/JSEN.2018.2864539.

[39] Yu Wu et al. "Electrical Impedance Tomography for Biomedical Applications: Circuits and Systems Review". In: *IEEE Open Journal of Circuits and Systems* 2 (2021), pp. 380–397. ISSN: 2644-1225. DOI: 10.1109/OJCAS.2021.3075302.

[40] Robert Pikkemaat et al. "Recent Advances in and Limitations of Cardiac Output Monitoring by Means of Electrical Impedance Tomography". In: *Anesthesia & Analgesia* 119.1 (July 2014), p. 76. ISSN: 0003-2999. DOI: 10.1213/ANE.0000000000000241.

[41] James Avery et al. "A Versatile and Reproducible Multi-Frequency Electrical Impedance Tomography System". In: *Sensors* 17.2 (Feb. 2017). Publisher: Multidisciplinary Digital Publishing Institute, p. 280. ISSN: 1424-8220. DOI: 10.3390/s17020280.

[42] Vinko Tomicic and Rodrigo Cornejo. "Lung monitoring with electrical impedance tomography: technical considerations and clinical applications". In: *Journal of Thoracic Disease* 11.7 (July 2019), pp. 3122–3135. ISSN: 2072-1439. DOI: 10.21037/jtd.2019.06.27.

[43] Bryan R Loyola et al. "Detection of spatially distributed damage in fiber-reinforced polymer composites". In: *Structural Health Monitoring* 12.3 (May 1, 2013). Publisher: SAGE Publications, pp. 225–239. ISSN: 1475-9217. DOI: 10.1177/1475921713479642.

[44] Bryan R. Loyola et al. "Spatial Sensing Using Electrical Impedance Tomography". In: *IEEE Sensors Journal* 13.6 (June 2013), pp. 2357–2367. ISSN: 1558-1748. DOI: 10.1109/JSEN.2013.2253456.

[45] Wahyu Lestari et al. "Sensing uniaxial tensile damage in fiber-reinforced polymer composites using electrical resistance tomography". In: *Smart Materials and Structures* 25.8 (July 2016). Publisher: IOP Publishing, p. 085016. ISSN: 0964-1726. DOI: 10.1088/0964-1726/25/8/085016.

[46] Lukas Heinzlmeier et al. "Damage evaluation in plain-woven CFRP plate with circular hole under cyclic tensile loading using electrical impedance tomography". In: *Structural Health Monitoring* (Nov. 13, 2024). Publisher: SAGE Publications, p. 14759217241284972. ISSN: 1475-9217. DOI: 10.1177/14759217241284972.

[47] Xiaoying Cheng et al. "Detection of indentation damage in carbon fibre-reinforced composites via EIT based on mechanical-electric coupling simulation and BT-CNN". In: *Nondestructive Testing and Evaluation* 0.0 (). Publisher: Taylor & Francis _eprint: https://doi.org/10.1080/10589759.2025.2553744, pp. 1–20. ISSN: 1058-9759. DOI: 10.1080/10589759.2025.2553744.

[48] Monica Sannamani et al. "Damage detection in non-planar carbon fiber-reinforced polymer laminates via electrical impedance tomography with surface-mounted electrodes and directional sensitivity matrices". In: *Composites Science and Technology* 224 (June 16, 2022), p. 109429. ISSN: 0266-3538. DOI: 10.1016/j.compscitech.2022.109429.

[49] A. J. Thomas et al. "Damage detection in self-sensing composite tubes via electrical impedance tomography". In: *Composites Part B: Engineering* 177 (Nov. 15, 2019), p. 107276. ISSN: 1359-8368. DOI: 10.1016/j.compositesb.2019.107276.

[50] Yening Shu et al. "Multi-Defect Detection in Additively Manufactured Lattice Structures Using 3D Electrical Resistance Tomography". In: *Sensors* 22.23 (Jan. 2022). Publisher: Multidisciplinary Digital Publishing Institute, p. 9167. ISSN: 1424-8220. DOI: 10.3390/s22239167.

[51] Tyler N. Tallman et al. "Damage mapping via electrical impedance tomography in complex AM shapes using mixed smoothness and Bayesian regularization". In: *Computer Methods in Applied Mechanics and Engineering* 414 (Sept. 1, 2023), p. 116185. ISSN: 0045-7825. DOI: 10.1016/j.cma.2023.116185.

[52] Adam K. Hussain et al. "Non-Destructive Testing of In-Situ Activated Fiber Reinforced Composites". In: ASME 2025 Aerospace Structures, Structural Dynamics, and Materials Conference. American Society of Mechanical Engineers Digital Collection, June 11, 2025. DOI: 10.1115/SSDM2025-152331.

[53] Jyrki Jauhiainen et al. "Nonplanar sensing skins for structural health monitoring based on electrical resistance tomography". In: *Computer-Aided Civil and Infrastructure Engineering* 36.12 (2021). _eprint: https://onlinelibrary.wiley.com/doi/pdf/10.1111/mice.12689, pp. 1488–1507. ISSN: 1467-8667. DOI: 10.1111/mice.12689.

[54] Tyler N. Tallman. "Conductivity-Based Nanocomposite Structural Health Monitoring via Electrical Impedance Tomography." Accepted: 2015-05-14T16:27:54Z. Thesis. 2015.

[55] Nuutti Hyvonen. "Complete Electrode Model of Electrical Impedance Tomography: Approximation Properties and Characterization of Inclusions". In: *SIAM journal on applied mathematics* 64.3 (2004). Place: Philadelphia Publisher: Society for Industrial and Applied Mathematics, pp. 902–931. ISSN: 0036-1399. DOI: 10.1137/S0036139903423303.

[56] Tyler N Tallman and Danny J Smyl. "Structural health and condition monitoring via electrical impedance tomography in self-sensing materials: a review". In: *Smart Materials and Structures* 29.12 (Oct. 2020). Publisher: IOP Publishing, p. 123001. ISSN: 0964-1726. DOI: 10.1088/1361-665X/abb352.

[57] Ethan K Murphy et al. "Phantom experiments using soft-prior regularization EIT for breast cancer imaging". In: *Physiological Measurement* 38.6 (May 2017). Publisher: IOP Publishing, p. 1262. ISSN: 0967-3334. DOI: 10.1088/1361-6579/aa691b.

[58] Bo Gong et al. "Sparse regularization for EIT reconstruction incorporating structural information derived from medical imaging". In: *Physiological Measurement* 37.6 (May 2016). Publisher: IOP Publishing, p. 843. ISSN: 0967-3334. DOI: 10.1088/0967-3334/37/6/843.

[59] T. N. Tallman and J. A. Hernandez. "The effect of error and regularization norms on strain and damage identification via electrical impedance tomography in piezoresistive nanocomposites". In: *NDT & E International* 91 (Oct. 1, 2017), pp. 156–163. ISSN: 0963-8695. DOI: 10.1016/j.ndteint.2017.07.003.

[60] A Borsic and A Adler. "A primaldual interior-point framework for using the L1 or L2 norm on the data and regularization terms of inverse problems". In: *Inverse Problems* 28.9 (Aug. 2012). Publisher: IOP Publishing, p. 095011. ISSN: 0266-5611. DOI: 10.1088/0266-5611/28/9/095011.

[61] Tyler N. Tallman et al. "The Effect of Different Regularization Approaches on Damage Imaging via Electrical Impedance Tomography". In: *Journal of Nondestructive Evaluation* 44.2 (Apr. 1, 2025), p. 41. ISSN: 1573-4862. DOI: 10.1007/s10921-025-01178-w.

[62] W. R. B. Lionheart. "Conformal uniqueness results in anisotropic electrical impedance imaging". In: *Inverse Problems* 13.1 (Feb. 1997), p. 125. ISSN: 0266-5611. DOI: 10.1088/0266-5611/13/1/010.

[63] Juan-Felipe P. J. Abascal et al. "Use of anisotropic modelling in electrical impedance tomography; Description of method and preliminary assessment of utility in imaging brain function in the adult human head". In: *NeuroImage* 43.2 (Nov. 1, 2008), pp. 258–268. ISSN: 1053-8119. DOI: 10.1016/j.neuroimage.2008.07.023.

[64] G. Belingardi, S. Boria, and J. Obradovic. "Energy Absorbing Sacrificial Structures Made of Composite Materials for Vehicle Crash Design". In: *Dynamic Failure of Composite and Sandwich Structures*. Ed. by Serge Abrate, Bruno Castanié, and Yapa D. S. Rajapakse. Dordrecht: Springer Netherlands, 2013, pp. 577–609. ISBN: 978-94-007-5329-7. DOI: 10.1007/978-94-007-5329-7_13.

[65] Cristiano Fragassa, Ana Pavlovic, and Giangiacomo Minak. “On the structural behaviour of a CFRP safety cage in a solar powered electric vehicle”. In: *Composite Structures* 252 (Nov. 15, 2020), p. 112698. ISSN: 0263-8223. DOI: 10.1016/j.compstruct.2020.112698.

[66] W. Van Paepegem et al. “Blast performance of a sacrificial cladding with composite tubes for protection of civil engineering structures”. In: *Composites Part B: Engineering*. Damage Mechanics 65 (Oct. 1, 2014), pp. 131–146. ISSN: 1359-8368. DOI: 10.1016/j.compositesb.2014.02.004.

[67] Mustapha Assarar et al. “Improving the damping properties of carbon fibre reinforced composites by interleaving flax and viscoelastic layers”. In: *Composites Part B: Engineering* 152 (Nov. 1, 2018), pp. 248–255. ISSN: 1359-8368. DOI: 10.1016/j.compositesb.2018.07.010.